



Space Weather®

L

RESEARCH ARTICLE

10.1029/2024SW003916

Key Points:

- We introduce an ionospheric model validation technique using SuperDARN ground backscatter
- Performance of the IRI-2016 is best during the daytime of January 2014 and 2018, whilst sporadic-E in June causes significant degradations
- IRI-2016 range errors are seen to be most significant near the terminator and during the nighttime

Correspondence to:

J. J. Ruck, jxr879@student.bham.ac.uk

Citation:

Ruck, J. J., Themens, D. R., Ponomarenko, P., Burrell, A. G., Kunduri, B., Ruohoniemi, J. M., & Elvidge, S. (2024). On the use of SuperDARN ground backscatter measurements for ionospheric propagation model validation. *Space Weather*, 22, e2024SW003916. https://doi.org/10.1029/2024SW003916

Received 8 MAR 2024 Accepted 14 AUG 2024

On the Use of SuperDARN Ground Backscatter Measurements for Ionospheric Propagation Model Validation

Joshua J. Ruck¹, David R. Themens^{1,2}, Pasha Ponomarenko³, Angeline G. Burrell⁴, Bharat Kunduri⁵, J. Michael Ruohoniemi⁵, and Sean Elvidge¹

¹Space Environment and Radio Engineering (SERENE) Group, School of Engineering, University of Birmingham, Birmingham, UK, ²Department of Physics, University of New Brunswick, Fredericton, NB, Canada, ³Institute of Space and Atmospheric Studies, University of Saskatchewan, Saskatoon, SK, Canada, ⁴Space Science Division, US Naval Research Laboratory, Washington, DC, USA, ⁵Bradley Department of Electrical and Computer Engineering, Virginia Tech, Blacksburg, VA, USA

Abstract Prior to use in operational systems, it is essential to validate ionospheric models in a manner relevant to their intended application to ensure satisfactory performance. For Over-the-Horizon radars (OTHR) operating in the high-frequency (HF) band (3-30 MHz), the problem of model validation is severe when used in Coordinate Registration (CR) and Frequency Management Systems (FMS). It is imperative that the full error characteristics of models is well understood in these applications due to the critical relationship they impose on system performance. To better understand model performance in the context of OTHR, we introduce an ionospheric model validation technique using the oblique ground backscatter measurements in soundings from the Super Dual Auroral Radar Network (SuperDARN). Analysis is performed in terms of the F-region leading edge (LE) errors and assessment of range-elevation distributions using calibrated interferometer data. This technique is demonstrated by validating the International Reference Ionosphere (IRI) 2016 for January and June in both 2014 and 2018. LE RMS errors of 100-400 km and 400-800 km are observed for winter and summer months, respectively. Evening errors regularly exceeding 1,000 km across all months are identified. Ionosonde driven corrections to the IRI-2016 peak parameters provide improvements of 200-800 km to the LE, with the greatest improvements observed during the nighttime. Diagnostics of echo distributions indicate consistent underestimates in model NmF2 during the daytime hours of June 2014 due to offsets of -8° being observed in modeled elevation angles at 18:00 and 21:00 UT.

Plain Language Summary Models of the ionized upper atmosphere, a region known as the ionosphere, must be validated using appropriate techniques prior to their use in operational systems. This is of greatest importance for Over-the-Horizon radars (OTHR) that rely on the reflection of radio waves in the 3–30 MHz band from the ionosphere for their operation. The accuracy of OTHR is largely related to the performance of the model ionosphere used to establish target positions, and so it is essential to understand how models behave under different circumstances. We introduce a new technique for validating models using measurements from the Super Dual Auroral Radar Network (SuperDARN) of research radars. Using a dominant feature present within these radar echoes, we perform an example validation of the International Reference Ionosphere (IRI) 2016 by modeling the expected path of radio waves. The performance is seen to be best during winter and typically worse in the evening. Using further information present within the measurements, we diagnose the likely cause of errors to be due to underestimates in a key model parameter. This is confirmed when we offset model parameters using direct measurements of the ionosphere and observe a significant improvement in model performance.

1. Introduction

By operating in the high-frequency (HF) band (3–30 MHz), radars can regularly see beyond the horizon, with ground ranges exceeding 3,500 km (Thayaparan et al., 2020) in some cases. This beyond line-of-sight (BLOS) propagation is achieved through the use of the ionosphere as a reflector, as within the HF band, this region of the upper atmosphere is refractive and has a profound impact on the path of radio waves. Over-the-horizon radar (OTHR) systems exploit this phenomenon and are unique in their ability to detect targets at extreme ranges, offering an effective solution to the problem of wide-area surveillance.

© 2024. The Author(s).

This is an open access article under the terms of the Creative Commons

Attribution-NonCommercial-NoDerivs

License, which permits use and distribution in any medium, provided the original work is properly cited, the use is non-commercial and no modifications or adaptations are made.

RUCK ET AL. 1 of 25

15427390, 2024, 9, Downloaded from https://agupubs.onlinelibrary.wiley.com/doi/10.1029/2024SW003916, Wiley Online Library on [02/05/2025]. See the Terms and Condition

conditions) on Wiley Online Library for rules of use; OA articles are governed by the applicable Creative Commons License

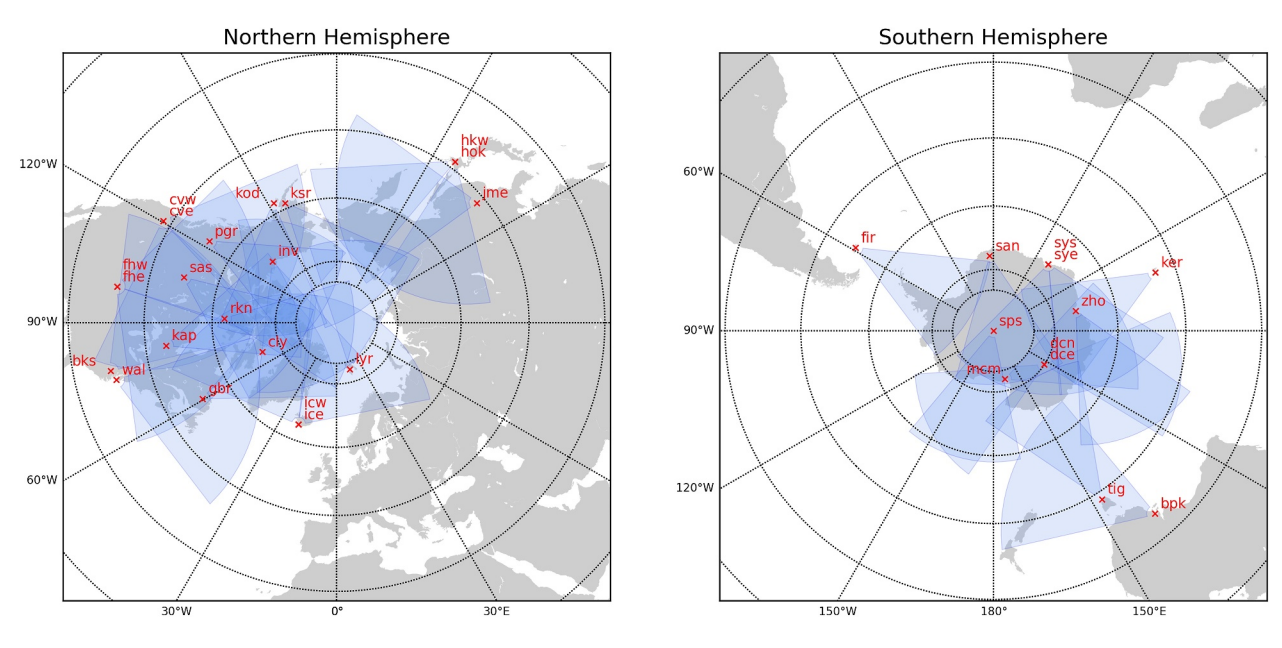


Figure 1. SuperDARN geographical coverage maps for a ground range of 3,500 km for all active radars as of January 2024. Lines of constant latitude are plotted at 15° intervals.

For the successful design and operation of HF systems, it is often essential to model HF propagation, and this is achieved through the combination of a suitable ionospheric model and raytracing solution. The positional accuracy of OTHR target detections is entirely beholden to the representativeness of the ionospheric specification on the immediate ionosphere. HF modeling is required to perform coordinate transforms from slant coordinates to geographical positions and to associate multipath echoes with the correct scatterers. This process is known as coordinate registration (CR) and forms a critical system of any OTHR (Fabrizio, 2013). For this, real time ionospheric models (RTIMs) are employed that assimilate the most up to date measurements of the ionosphere (Fabrizio, 2013; Fridman et al., 2012). Providing a suitable ray tracer is employed, propagation errors, and thus CR positioning errors, can largely be attributed to shortcomings in the specification of the bottomside ionosphere. Due to the large dependence of OTHR accuracy on the ionospheric model employed, it is therefore paramount to understand the performance and error behaviors of models prior to use in operational CR systems if accurate and reliable OTHR target positioning is to be expected.

Typical validation methods for assessing ionospheric models include examination of peak density parameters (Shim et al., 2011; Themens et al., 2017), integrated profile densities (Chen et al., 2020; Chou et al., 2023; Themens & Jayachandran, 2016) and topside in situ satellite densities (Shim et al., 2012; Themens, Jayachandran, & McCaffrey, 2019). In the context of the oblique propagation encountered in many HF systems, these techniques are of limited suitability as they provide little insight to the cumulative effect of ionospheric density gradients on HF ray paths which are limited to the bottomside ionosphere. Validation efforts must assess the full climatology and latitudinal structuring of the ionosphere if a truly holistic assessment is to be made. Furthermore, typical OTHR measurements such as backscatter soundings that may provide an alternative avenue are often highly restricted due to the classified nature of systems. A relatively dense global data set of publicly available oblique HF soundings covering at least a full solar cycle are required to facilitate the global validation of ionospheric models. For the real time ionospheric models (RTIMs) employed in operational OTHR systems, suitable validation should also be capable of assessing the model at high cadences besides just assessing climatological performance. Validation of models with consideration to all these factors necessitates the development of new model assessment techniques.

The Super Dual Auroral Radar Network (SuperDARN) is a network of HF coherent scatter research radars operating in the range of 8–20 MHz (Chisham et al., 2007; Greenwald et al., 1995; Nishitani et al., 2019) that provides a suitable data set. Over 35 SuperDARN radars are distributed across both hemispheres at latitudes poleward from 30° either side of the equator as shown in Figure 1. This expansive deployment provides an unparalleled coverage of ionospheric plasma dynamics at mid-to high-latitudes. The wide azimuthal field of view

RUCK ET AL. 2 of 25

15427990, 2024, 9, Downloaded from https://agupubs.onlinelibrary.wiley.com/doi/10.1029/2024SW003916, Wiley Online Library on [02/05/2025]. See the Terms and Conditions (https://onlinelibrary.wiley.com/terms-and-conditions)

ons) on Wiley Online Library for rules of use; OA articles are governed by the applicable Creative Commons Licenso

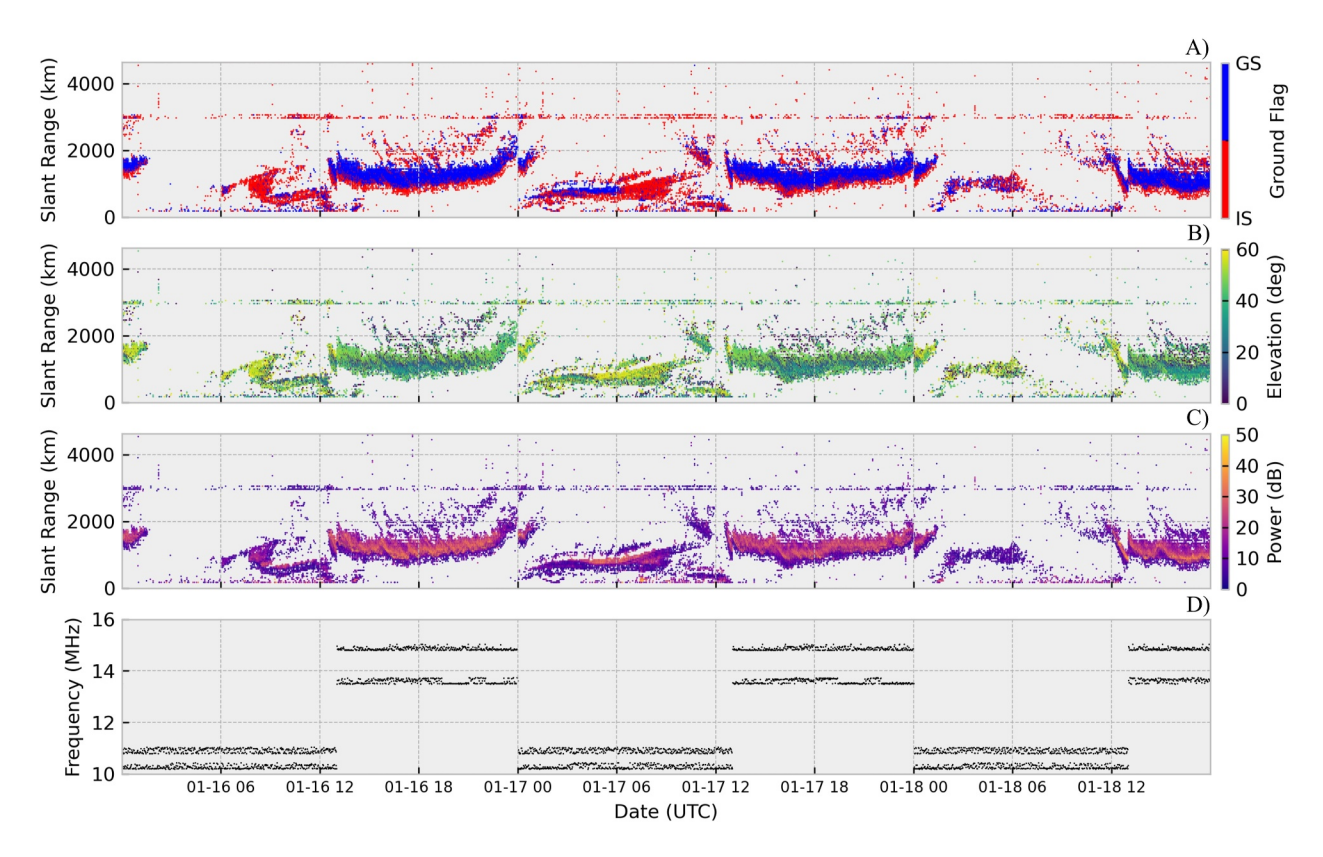


Figure 2. Summary data plot for the Blackstone radar Beam 16 between 16th and 18th January 2014, showing a dominating presence of ground backscatter echoes and the operation of the radar in a dual frequency sounding mode. The presented ground flags (a) are from the standard SuperDARN fitted files and no manual flagging has been performed. Panel (b) shows the backscatter elevation angle of arrival estimates by the SuperDARN interferometer array calculated using the standard Tdiff estimate provided in the hardware data file for the Blackstone radar without calibration. Panel (c) provides signal-to-noise ratio values from the SuperDARN ACF estimation whilst panel (d) presents the transmission frequency.

(FOV) of the radars, often between 51.84° and 77.76°, combined with OTH propagation permits even single SuperDARN radars to cover vast geographic areas. Measurements with radars of the SuperDARN design have been conducted since the first radar was installed in 1983 at Goose Bay in Canada (Greenwald et al., 1985) and are regularly performed in real time at most of the radar sites, thus offering an expansive data set of backscatter data.

Whilst signals backscattered by field aligned ionospheric irregularities are of primary interest to much of the community due to the information they provide on bulk plasma drifts, a significant proportion of the data provided by SuperDARN soundings is of ground/sea backscatter (GS) origin. GS echoes can typically be distinguished from ionospheric scatter (IS) due to their near zero doppler shift and spectral width that are both characteristically different from IS (Ponomarenko et al., 2007), and so can provide a useful secondary measurement within SuperDARN soundings. It is worth noting that at times, very slow moving IS may be improperly flagged by the SuperDARN processing procedures and can pollute GS echoes. An example summary plot of backscatter from the Blackstone SuperDARN radar beam 16 for the time period 16th to 19th January 2014 is demonstrated in Figure 2, showing the presence of GS echoes. This beam is 14.58° from boresight at zero elevation and corresponds to a bearing of -25.42° as presented in Figure 3 and is the focus of this paper. We use the standard SuperDARN convention of zero-indexing when referring to beam numbers.

GS measurements have found increasing utility over time, showing use for interferometer calibration (Jiang et al., 2022; Ponomarenko et al., 2015, 2018) and real time determination of ionospheric parameters including foF2 (Bland et al., 2014) and maximum useable frequency (MUF) (Hughes et al., 2002). Climatological studies using GS data have also been performed by Ponomarenko et al. (2010), Ponomarenko and McWilliams (2023), Oinats et al. (2016) and Koustov et al. (2022) to determine occurrence rates, with Ponomarenko et al. (2010) additionally assessing the impact of the underlying ground scattering surface and the presence of sea ice.

RUCK ET AL. 3 of 25

15427390, 2024, 9, Downloaded from https://agupubs.onlinelibrary.wiley.com/doi/10.1029/2024SW003916, Wiley Online Library on [02/05/2025]. See the Terms and Conditions (https://onlinelibrary.wiley.com/doi/10.1029/2024SW003916, Wiley Online Library on [02/05/2025]. See the Terms and Conditions (https://onlinelibrary.wiley.com/doi/10.1029/2024SW003916, Wiley Online Library on [02/05/2025]. See the Terms and Conditions (https://onlinelibrary.wiley.com/doi/10.1029/2024SW003916, Wiley Online Library on [02/05/2025]. See the Terms and Conditions (https://onlinelibrary.wiley.com/doi/10.1029/2024SW003916, Wiley Online Library on [02/05/2025]. See the Terms and Conditions (https://onlinelibrary.wiley.com/doi/10.1029/2024SW003916, Wiley Online Library on [02/05/2025]. See the Terms and Conditions (https://onlinelibrary.wiley.com/doi/10.1029/2024SW003916, Wiley Online Library on [02/05/2025]. See the Terms and Conditions (https://onlinelibrary.wiley.com/doi/10.1029/2024SW003916, Wiley Online Library.wiley.com/doi/10.1029/2024SW003916, Wiley Online Library.wiley.com/doi/10

and-conditions) on Wiley Online Library for rules of use; OA articles are governed by the applicable Creative Commons License

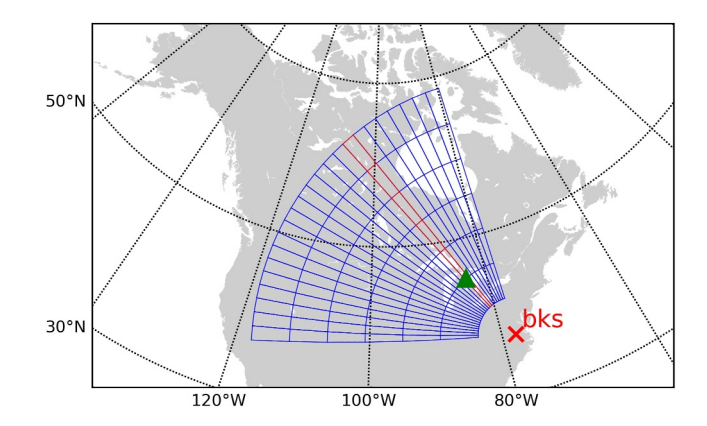


Figure 3. Geographical coverage of the Blackstone radar's 24 beams spaced at 3.24°. Markers are provided in ground range for intervals of 500 km. Beam 16 is indicated in red with the Alpena ionosonde marked downrange by a green triangle.

Significant research has also been conducted on using SuperDARN GS to observe Traveling Ionospheric Disturbances (TIDs) through the quasiperiodic variations they impart to backscatter time series. Examples of detecting TIDs include Oinats et al. (2015) and Karhunen et al. (2006) use of minimum GS range variations, Bristow et al. (1994) use of echo power fluctuations from focusing/defocussing, Hayashi et al. (2010) use of doppler velocity variations, and Samson et al. (1990) and Frissell et al. (2014) use of the multiple signal classification (MUSIC) algorithm on range-time echo power data. Climatological studies have been performed on TIDs using SuperDARN by a range of authors, for example, Frissell et al. (2014) and Hayashi et al. (2010) for Medium-scale and Large-scale TIDs, respectively. In a similar manner to Hayashi et als (2010), Nishitani et al. (2011) use the doppler signatures to instead detect seismic-induced ionospheric disturbances. Further applications of SuperDARN GS include analysis of shortwave fadeout events by Chakraborty et al. (2018) and derivation of ionospheric winds by Theurer and Bristow (2017).

HF propagation modeling may be used to represent the expected signal paths of GS echoes present within SuperDARN backscatter, where differences may be

predominantly attributed to the ionospheric model. By modeling this data over a range of time periods and geographical areas, it is possible to make comparisons between simulated SuperDARN GS echoes and those present within the actual data set to gain a rigorous understanding of shortcomings in the model. By generalizing this approach, the technique may be applied to any SuperDARN radar in the network, thus unlocking almost all of the available SuperDARN GS data. Other HF radars with similar data sets may also provide candidate validation opportunities.

A dominant feature within backscatter time series is that of the leading-edge (LE), which corresponds to the skip distance. This may be used to make direct comparisons between the SuperDARN radar and modeled data sets. This provides partial information regarding foF2, hmF2, and F-peak thickness when combined with elevation angle measurements. To the first order, the group leading-edge distance, P_{\min} , is

$$P_{\min} = \frac{2h_{\nu}}{\cos(\frac{\pi}{2} - \theta_{\max})} \tag{1}$$

that is a form of Martyn's theorem for a planar earth geometry and vertically stratified ionosphere, where h_{ν} is the virtual height of reflection and $\theta_{\rm max}$ is the maximum transmission elevation (Martyn, 1935). Here, the maximum elevation angle may be predicted by Snell's law under the same assumptions of Equation 1 when ignoring particle collisions and Earth's magnetic field using the following relation

$$N_{\text{max}} = \frac{f^2 \sin^2 \theta}{81} \tag{2}$$

Where $N_{\rm max}$ is the maximum electron density in m⁻³ and f is the transmission frequency in Hz (Davies, 1965). Further to the LE, the provision of elevation angle estimates permits assessment of echo distributions in group range-elevation space as an opportunity for model diagnostics. The analysis may also be extended to range-power space to test an alternative aspect of the propagation model; however, we restrict our initial analysis in this study to LE and elevation.

In this study, we introduce a comprehensive method for the validation of ionospheric models at minutely resolutions in a manner appropriate to OTHR and oblique HF systems in general by utilizing the vast data set offered by the SuperDARN radars. A SuperDARN simulator is first demonstrated in Section 2.1 utilizing two-dimensional numerical ray tracing (NRT) with inclusion of power calculations using modeled antenna array patterns established in Section 2.2. Extensive data processing is then performed in Section 2.3 to permit proper comparisons between model and experimental data. We then perform an example assessment of the International Reference Ionosphere 2016 (IRI-2016) using this method, including analysis of LE variations in Sections 3.1 and 3.2, comparison of echo elevation-range distributions in Section 3.3, testing of simulated backscatter using

RUCK ET AL. 4 of 25

15427390, 2024, 9, Downloaded from https://agupubs.onlinelibrary.wiley.com/doi/10.1029/2024SW003916, Wiley Online Library on [02/05/2025]. See the Terms and Condition

ons) on Wiley Online Library for rules of use; OA articles are governed by the applicable Creative

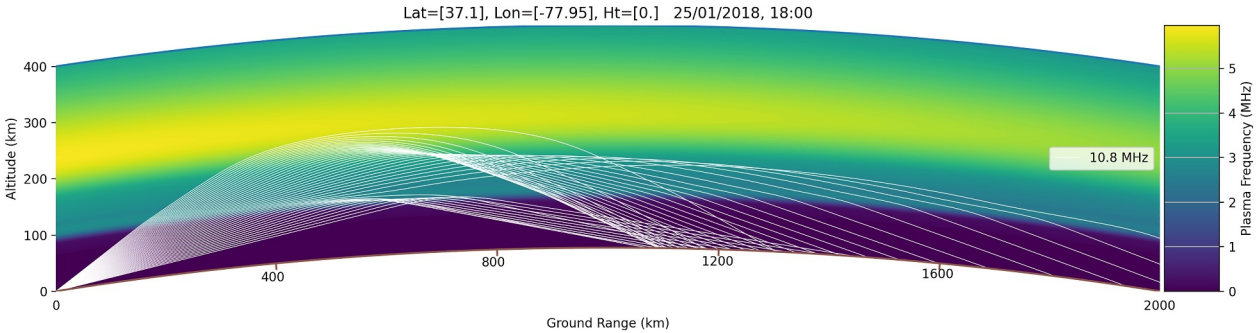


Figure 4. Example raytrace using HFRM for the Blackstone radar beam 16 at 18:00 UT on the 25th Jan 2018, showing distinct propagation modes via different regions of the ionosphere. Transmission frequency is set to 10.8 MHz

ionosonde driven peak density parameters in Section 3.4, and diagnosis of model errors in Section 3.5 using echo elevation-range distributions simulated with offsets to NmF2, hmF2 and the interferometer calibration parameter, $T_{\rm diff}$. Our analysis is applied herein across the months of January and June in both 2014 and 2018 to encompass summer and winter periods during active and quiet phases of the solar cycle.

2. Methodology and Propagation Model

2.1. HF Raytracing

NRT is a technique widely employed to study HF propagation through the ionosphere and is well suited for simulating SuperDARN backscatter. NRT has been previously used by Perry et al. (2022) for example, in the context of SuperDARN to validate the Saskatoon radar's gain pattern. This study makes use of the HFRM (highfrequency raytracing model) 2D NRT toolbox developed by the University of Birmingham's Space Environment and Radio Engineering (SERENE) group and is used to model the expected signal paths for the Blackstone radar beam 16 with the IRI-2016 ionospheric model. It should be noted that the choice of ionospheric model and beam is arbitrary and used only for demonstration of this technique, which may be applied broadly to any beam and ionospheric model as appropriate. An example 2D ray trace for this beam simulated using HFRM is presented in Figure 4. HFRM has previously been employed by SERENE to model multi-static OTHR and uses an improved version of the NRT ray tracer detailed in the work of Coleman (1998), which is based on the Haselgrove set of equations (Haselgrove, 1955).

2D ionospheric grids are generated using the IRI once every 15 min and linearly interpolated down to the minutely resolution of the SuperDARN data. Whilst this is in excess of the model resolution, a finer generation time step is included to permit future work with assimilative models that operate with greater temporal resolutions. At each time step within the SuperDARN data, a total of 350 rays are propagated at elevations between 5° and 60° with frequency set to match that of the data. Ray landing points are then extracted and binned by group range into the same range gate bins as for the SuperDARN data.

Due to the conic beam structure of linear arrays, non-boresight beams are spread in azimuth as the pointing direction of the main lobe varies with elevation (Shepherd, 2017). The SuperDARN array phasing matrices are configured to form beams at specific azimuths at zero elevation, and so at higher elevations there is always a mismatch between the stated beam direction and the true propagation direction. This effect is most significant for higher elevations and beams further from boresight. For the 2D NRT ray tracer utilized in this study, we restrict propagation to a great circle slice in the direction of the zero-elevation beam azimuth. This is a minor limitation of our technique as the modeled rays will transition through a different geographical region of the ionospheric model than the real ionosphere. We do not consider this limitation a significant hindrance to our current analysis as Fregion echoes are the focus of this study that typically arrive at lower elevation angles often below approximately 45° where the conic beam deviations are less pronounced. This is demonstrated in the following section. Beyond this, 2D NRT is only suitable for weak horizontal gradients as the technique is unable to capture off great circle ray deviations that cause rays to transition different geographical regions. For the reasons detailed here, 2D NRT

RUCK ET AL. 5 of 25 when using great circle ionospheres is only recommended for near boresight beams and conditions where large density gradients are not expected.

To calculate the backscattered power for a given ray, a form of the radar equation must be used and is given by the following (Coleman, 1997):

$$P_r = \frac{P_T G_T G_R}{(4\pi)^3 d_T^2 d_R^2} \frac{\lambda^2 A_{eff} \sigma_0}{L_T L_R L_{Pol}}$$
(3)

Where P_T is the transmitted power, G_T and G_R the transmit and receive antenna gains, λ the wavelength, A_{eff} the effective scattering area, σ_0 the backscatter coefficient, d_T and d_R the effective distance along the transmit and receive rays, L_T and L_R the attenuation factor due to ionospheric absorption on the transmit and receive rays, and L_{Pol} is the polarisation mismatch at the receive array. Here, the effective distance represents both the group range of the ray flux tubes and the focusing/defocussing of them by the ionosphere (Coleman, 1997). We take L_{Pol} to be 3 dB in order to account for the average mismatch with the receive antenna due to the ray polarization upon exiting the ionosphere being unknown.

The effective area can be considered as the imposed area of a flux tube at the ground, and can be determined by the following equation (Slimming & Cervera, 2019):

$$A_{eff} = R_e \sin\left(\frac{D}{R_e}\right) \frac{dD}{d\theta} \Delta \theta \Delta \Phi \tag{4}$$

Where *D* is the ground range, $\Delta\theta$ is the ray fan elevation step, and $\Delta\Phi$ is the azimuthal beamwidth. Calculation of the $\frac{dD}{d\theta}$ term is performed for pairs of rays in a fan.

Deviative and non-deviative ionospheric absorption is calculated along the ray path for the case of no magnetic field using the following equation derived from the Appleton-Hartree equation when ignoring Earth's magnetic field (Davies, 1965):

$$L = \frac{4.34e^2}{\epsilon_0 m_e c} \int \frac{1}{\mu} \left(\frac{N_e v}{4\pi^2 f^2 + v^2} \right) dP \tag{5}$$

Where e is the charge of an electron, v the electron-neutral collision frequency, ϵ_0 the permittivity of free space, m_e the mass of an electron, c the speed of light in free space, μ the real refractive index, and P the group range. Collision frequency is calculated at each point on the ray path with electron density, neutral density and neutral temperature, with profiles for the latter two provided in Appendix A.

Backscatter losses vary widely depending on surface conductivity, roughness, terrain type as well as incidence angle, and it is known to be difficult to model due to the limited data sets available and the inherent difficulties with isolating the backscatter loss contribution. Studies of backscatter coefficients have been conducted around Australia using Jindalee Operational Radar Network backscatter sounders by Slimming and Cervera (2019), Edwards and Cervera (2022), and Edwards et al. (2022), with the latter demonstrating the variability of coefficients over different terrain conditions and the notably strong correlation with vegetation. For the purposes of this study, a backscatter coefficient of either -23 dB or -26 dB is simply used for backscatter from sea or land. A value of -23 dB is representative of a fully developed sea (Coleman, 1997; Munk & Nierenberg, 1969), whilst the value for land is an estimate based on the work of Edwards et al. (2022) for a 11%-30% coverage of woodland. Due to the large variations in land backscatter coefficients, it must be stressed that this is an approximate median value.

2.2. Antenna Array Modeling

The antenna array gain patterns and beamwidths for the beamformed array are required for calculation of power in Equations 3 and 4. Two antenna array designs are used by the SuperDARN network, with the older generation utilizing horizontal log-periodic dipole array (LPDA) elements, specifically the Sabre Communications

RUCK ET AL. 6 of 25

15427390, 2024, 9, Downloaded from https://agupubs.onlinelibrary.wiley.com/doi/10.1029/2024SW003916, Wiley Online Library on [02/05/2025]. See the Terms and Conditions (https://onlinelibrary.wiley

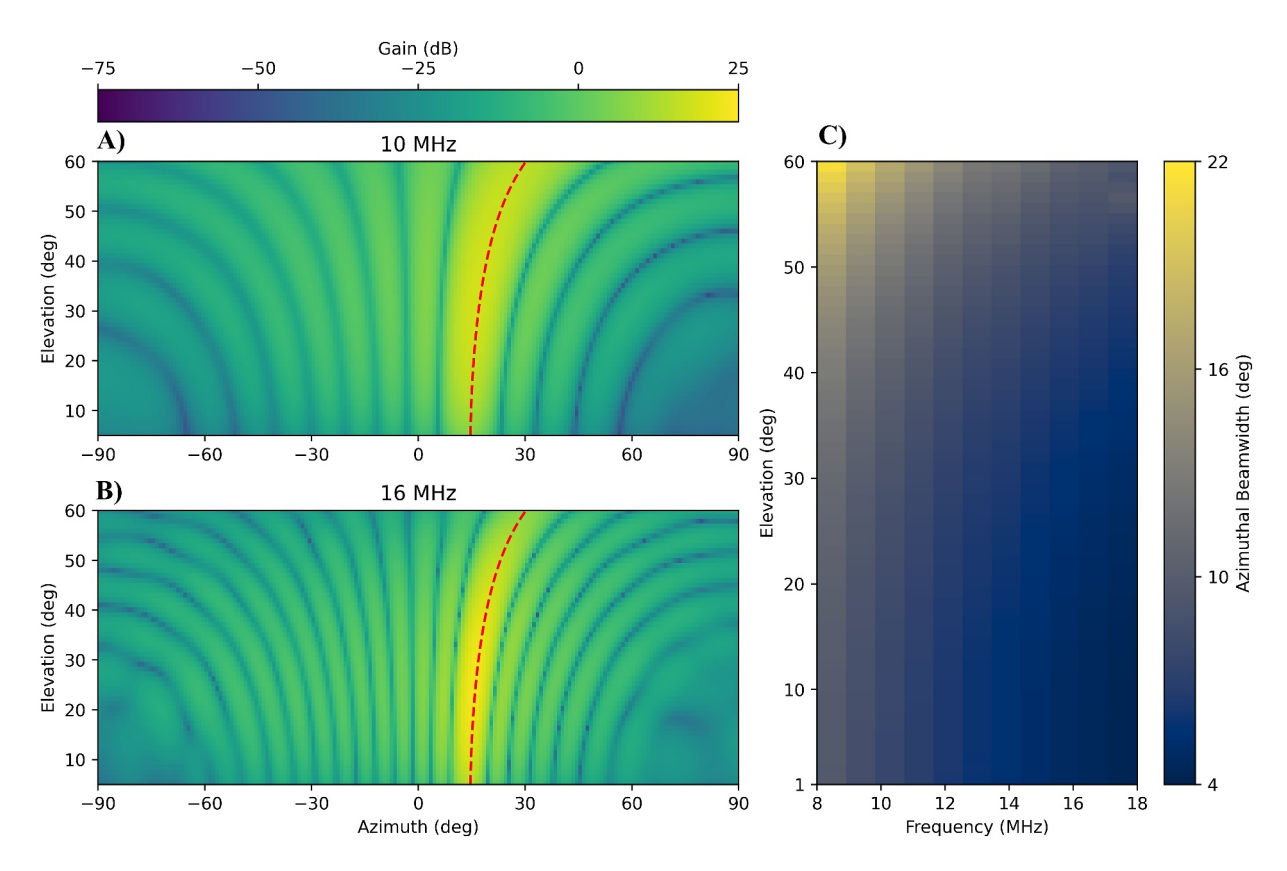


Figure 5. Radiation patterns for the TTFD array phased to beam 16 at 10 MHz (a) and 16 MHz (b). The variation in azimuthal beamwidth of the main lobe is provided in panel (c) for a range of frequencies. A red dashed line is plot in panels a and b to show the location of the main lobe profile used in this study. Azimuthal beamwidth is taken as the 3 dB width from this profile in the azimuthal axis at each elevation.

Corporation model 608 (Custovic et al., 2011), and the newer generation utilizing the novel twin terminated folded dipole (TTFD) elements (Sterne et al., 2011). Whilst gain pattern data for the TTFD antenna elements have been modeled by Custovic et al. (2011) and for the array by Sterne et al. (2011), numerical data was not provided. Data for beam 7 of the Saskatoon radar was provided by Perry et al. (2022); however, no other beams are provided.

To permit validation across the full SuperDARN network on any beam, we model gain patterns for each beam of the two antenna designs using the Numerical Electromagnetics Code (NEC) version 2. NEC is a software program for the modeling of thin wire antennas developed at the Lawrence Livermore National Laboratory by Burke and Poggio (1981). This program was selected due to its prior use by Custovic et al. (2011), Sterne et al. (2011) and Perry et al. (2022). Far field radiation patterns are generated at 1 MHz intervals for beam 16 of the TTFD array, respectively. This data is provided to the community in (Ruck, 2024a) along with data for beam 12 and 20. Elevation gain patterns for beam 16 of the Blackstone TTFD antenna array are presented in panel a and b of Figure 5, whilst the variation in azimuthal beamwidth with frequency and elevation is presented in panel c.

The direction of maximum gain is marked along the main lobe with a red dashed line in panels a and b to indicate the gain profiles used in this study and to demonstrate the extent of the previously mentioned variation of beam direction with elevation. For beam 16 considered here, this deviation does not exceed the beam width for the observed range of elevation angles (<50°), so that the beam's overlap with the field-of-view of the Alpena ionosonde is not affected in any significant way and the ray tracing slice is always within the main lobe.

Whilst a simple analytical relationship for beamwidth may be used for a linear array, we note the importance of including the elevation variation from the modeled gain patterns. A change between low and high elevations of 5° and 60° presents a doubling of beamwidth in Figure 5c and will directly introduce a 3 dB change in power through Equations 3 and 4.

RUCK ET AL. 7 of 25

15427390, 2024, 9, Downloaded from https://agupubs.onlinelibrary.wiley.com/doi/10.10292024\$W003916, Wiley Online Library on [02/05/2025]. See the Terms and Conditions (https://onlinelibrary.wiley.com/doi/10.10292024\$W003916, Wiley Online Library on [02/05/2025]. See the Terms and Conditions (https://onlinelibrary.wiley.com/doi/10.10292024\$W003916, Wiley Online Library on [02/05/2025]. See the Terms and Conditions (https://onlinelibrary.wiley.com/doi/10.10292024\$W003916, Wiley Online Library on [02/05/2025]. See the Terms and Conditions (https://onlinelibrary.wiley.com/doi/10.10292024\$W003916, Wiley Online Library on [02/05/2025].

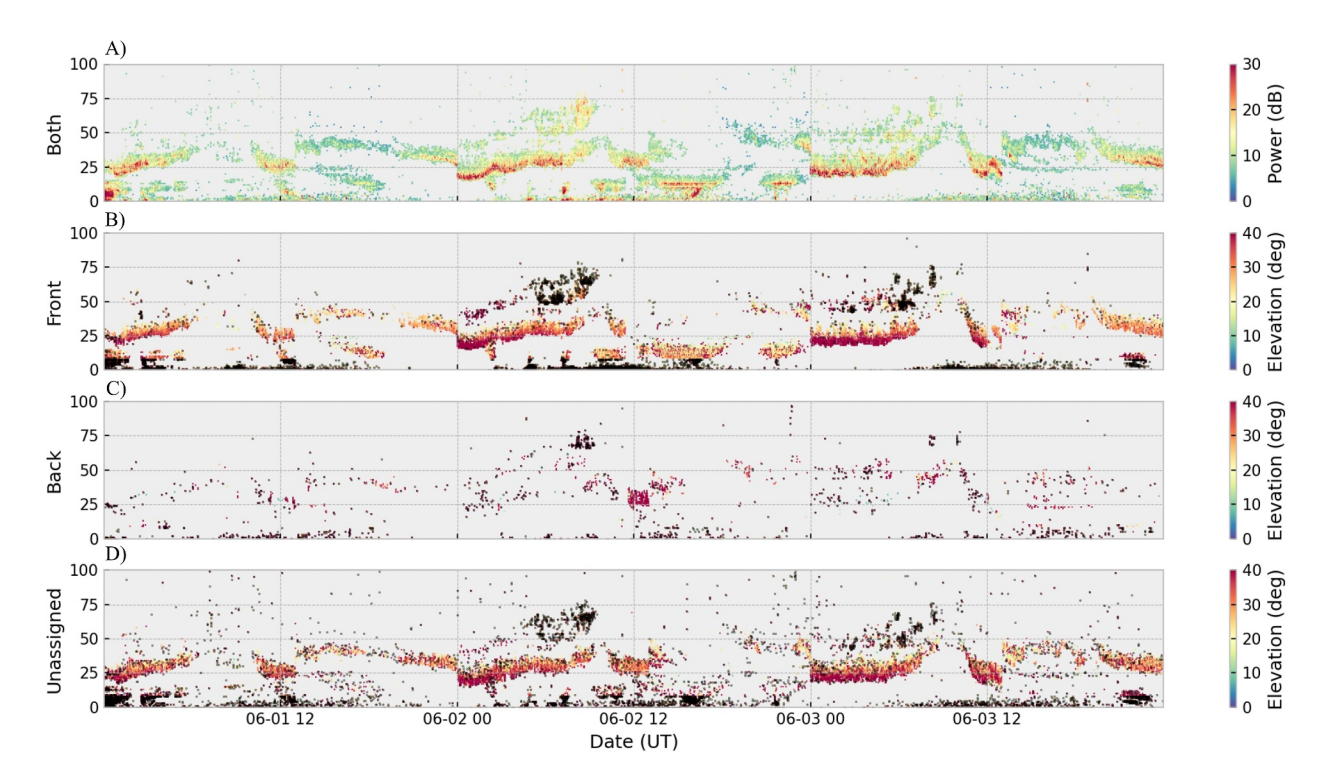


Figure 6. FOV assignments for Blackstone beam 16 using the Burrell et al. (2015) automatic FOV detection algorithm in June 2014, showing a significant proportion of echoes being unassigned. Elevation data is calculated using the default $T_{\rm diff}$ value in the Blackstone hardware data file for this period which was equal to the calibrated value. Echoes flagged as IS are marked by a black dot.

2.3. Data Processing

2.3.1. FOV Processing

Prior to performing validation, the SuperDARN and model data must first be conditioned to ensure proper comparisons can be made, as echoes exist within SuperDARN data that are not modeled using raytracing or are of ambiguous origin. These include echoes from meteor ionisation, sporadic-E, incorrectly assigned ionospheric scatter, and echoes originating from the rear FOV. The latter has been a long-understood problem for Super-DARN and is largely due to the relatively poor front to back ratio of the LPDA arrays and the fact that beamforming causes a secondary lobe behind the radar, meaning a non-negligible amount of power is radiated behind the radars (Milan et al., 1997). Due to this secondary source of echoes from behind the radars, it is important to determine if the echoes come from the main lobe or from behind the antenna array when performing validation with simulated echoes to ensure comparisons are consistent. In our application of the technique here, we remove any backscatter from behind the radar and focus on echoes from the front FOV. Based on the interferometric evidence of Milan et al. (1997), an automatic FOV detection algorithm was developed by Burrell et al. (2015) to assign correct FOVs and is included in this validation for radars using LPDA arrays. This algorithm is contained within the deprecated DavitPy Python package developed by Virginia Tech (Ribeiro et al., 2020) available from https://zenodo.org/records/3824466. Example FOV assignments are presented in Figure 6 for 1st-3rd June 2014, showing the assignment of most echoes to the front FOV as expected for the TTFD array. The FOV Algorithm was applied to radar scans that were of equal frequency, operating mode and channel. For the 39,783 echoes in this time period, we assign 46.68% of echoes to the front FOV, 5.26% to the rear FOV, and are left with 48.10% as unassigned.

Unfortunately, many echoes remain unassigned by the algorithm, and to avoid ambiguity, these should be removed in conjunction with the rear FOV and IS. It is expected that tuning of algorithm parameters may improve assignment rates for specific periods, as our implementation was tested using the examples in Burrell et al. (2015), which confirmed the algorithm performed as expected with low unassigned rates. The default values detailed in

RUCK ET AL. 8 of 25

Burrell et al. (2015) were used in this example, as it is beyond the scope of this work to optimize the parameters, which would otherwise prevent the liberal application of the validation technique. We do not use the FOV processing algorithm on the Blackstone data in our current work beyond a demonstration, as the TTFD corner reflector provides sufficient mitigation of rear echoes, but stress the importance of doing so when using a radar with LPDA design.

2.3.2. Elevation Calibration

Significant caution is warranted when utilizing SuperDARN elevation data as the often-unsuitable interferometer $T_{\rm diff}$ calibration values provided in radar hardware data files can produce non-physical elevation distributions that are not indicative of the real propagation environment. Significant efforts have been made to properly calibrate the radars in the last decade, and the reader is recommended to consult Chisham et al. (2021) for a full treatment of the methods available. For this work, we rely on the E-Region backscatter calibration technique of Ponomarenko et al. (2018) as it is capable of providing automated daily $T_{\rm diff}$ values across all historical data. The value of $T_{\rm diff}$ was found to change sporadically in January 2014 at the onset of significant noise in the Blackstone radar data and so several values were required to mitigate elevation errors here. The values used in this study are provided in Appendix A.

2.3.3. Echo Cluster Filtering

The principal interest of this study is 1F GS echoes, as these are clearly identifiable and regularly exhibit a higher power due to focusing at the boundary of the skip zone (Davies, 1965). We use the standard notation of 1F or 1E to refer to the propagation mode where the number refers to the total hops between the ionosphere and ground on a one-way path and the letter refers to the ionospheric region. Echoes reflected within the E-region by normal 1E-mode, Sporadic-E, Auroral-E, and meteor scatter are difficult to distinguish and so ambiguity exists over their origin, which provides an unreasonable source of error for validation as no current ionospheric model contains treatment of them. This necessitates the filtering of the data to remove these unwanted echoes that all lie at nearer range gates than that of the 1F mode.

Various virtual height models exist that aim characterize echo origins based on climatological SuperDARN data (Chisham et al., 2008; Thomas & Shepherd, 2022). These are unsuitable for our purpose, since they include no consideration of the temporal variability of these channels. Furthermore, using strict filter thresholds to define echo origins can introduce artificial leading-edge features that would degrade the LE analysis of this technique. A neural network-based characterization scheme was introduced by Kunduri et al. (2022) that offers potentially improved assignments at the expense of expected increased computation time. Conversely, filtering may be altogether avoided by directly extracting the LE using the fitting method introduced by Bland et al. (2014), yet this was not implemented as this would reduce the cadence of our validation due to the requirement to down sample data into 10–15-min windows. Furthermore, this method requires the radars to operate in a multi-frequency sounding mode, which limits the method to periods when this special control mode is being used.

Echoes from distinct propagation channels form temporally and spatially coherent structures in SuperDARN backscatter time series that are often clearly identifiable. We apply the Density-based spatial clustering of applications with noise (DBSCAN) algorithm (Ester et al., 1996) to both the model and SuperDARN data in virtual height–group range space in 30-min intervals. Virtual height is calculated using the following equation (Bland et al., 2014), which assumes straight line geometry using the distance to the reflection point r, which is equal to P/2 for ground scatter.

$$h_{\nu} = \sqrt{r^2 + R_e^2 + 2rR_e \sin \theta} - R_e \tag{6}$$

DBSCAN has previously been employed for SuperDARN backscatter characterization as part of Kunduri et al.'s (2022) machine learning framework with success. Echoes with elevations below and above 40° are clustered in separate instances, as this provides separation in cases where backscatter is observed across most range gates that may otherwise be incorrectly grouped. The data is clipped and normalized before the algorithm is

RUCK ET AL. 9 of 25

15427996, 2024. 9, Downloaded from https://agupubs.onlinelibrary.wiley.com/doi/10.1029/2024SW003916, Wiley Online Library on [02/05/2025]. See the Terms and Conditions (https://onlinelibrary.wiley.com/terms-and-conditions) on Wiley Online Library for rules of use; OA articles are governed by the applicable Creative Commons License

Table 1Cluster Centroid Filtering Thresholds for the Separate High and Low Elevation and Frequency Bands

	Low elevation		High elevation	
Frequency	Low	High	Low	High
Minimum centroid virtual height	150 km	150 km	125 km	125 km
Minimum centroid range	1,100 km	900 km	850 km	750 km

Note. Different parameters are used to tailor the filtering to the different echo regimes.

applied with a maximum neighborhood distance value of 0.07 that was determined through a quantitative assessment of all data in the current analysis using the recommended approach detailed in (Ester et al., 1996).

If less than 5 points are available in a given 30-min window, the data is removed as it is not possible to reliably determine the origin of such back-scatter using this clustering technique for such a small number of points. Filtering is applied to cluster centroids by removing clusters with virtual heights and group ranges falling below the thresholds in Table 1 for the low and high frequency nighttime and daytime operation, respectively. Echoes flagged as noise by DBSCAN are tested to examine if at least 2 neighboring points in a 3 \times 5 box are contained within an accepted cluster, with such points kept and those failing this criterion removed.

This approach removes the unwanted echoes providing they are contained within a coherent backscatter structure and Figure 7 shows the capacity of this method to process both model and Blackstone radar data. At times when the separation between near range echoes and the primary 1F group is small, these echoes may become clustered together, resulting in either both being removed or the non-1F echoes being kept. Furthermore, non-1F clusters whose centroids exceed the values in Table 1 are kept regardless of their origin. Whilst we recognize the limitations of our approach, the technique is sufficient for our application here and limits arbitrary modifications to the LE that may be imposed by alternative methods.

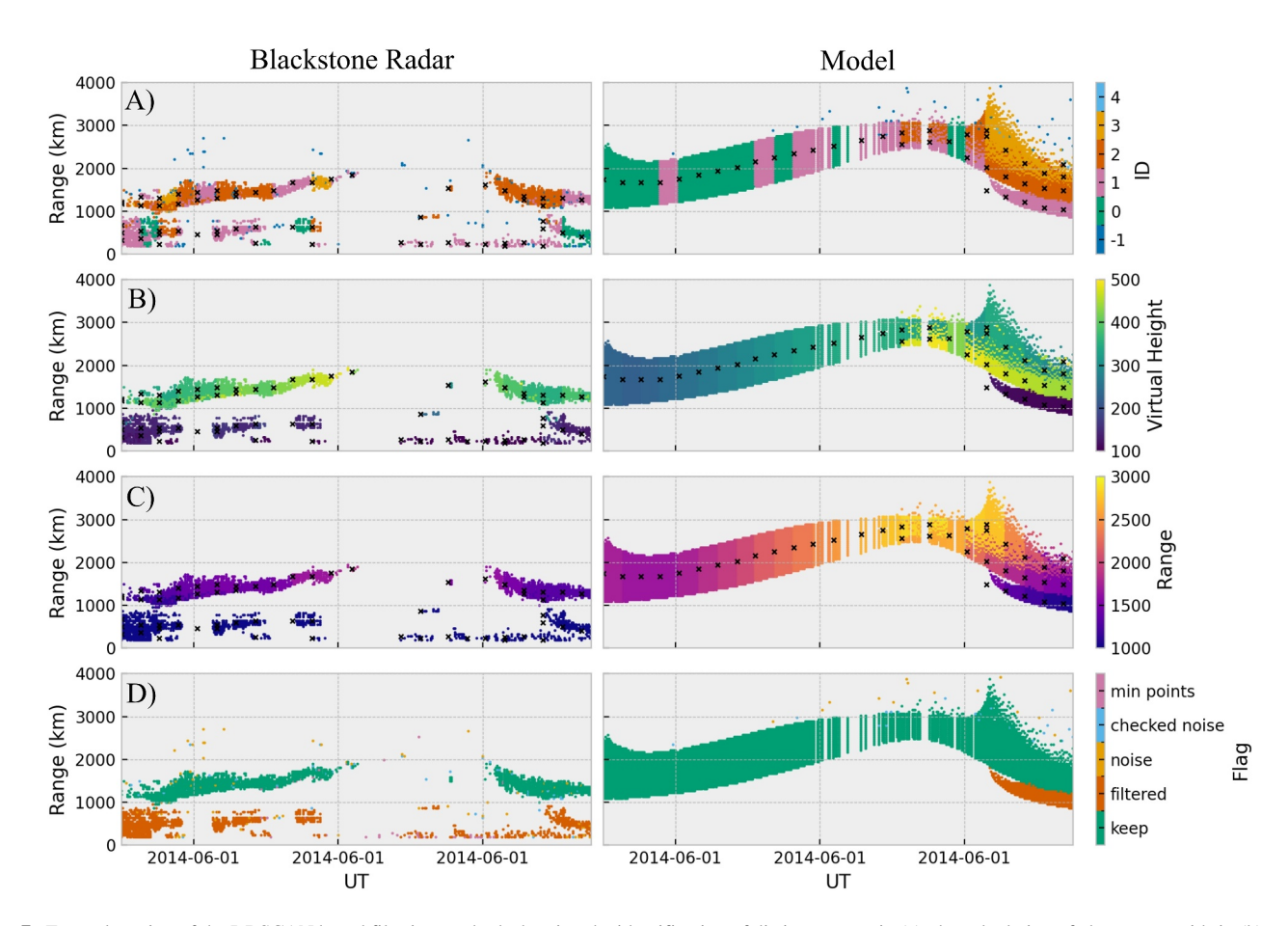


Figure 7. Example action of the DBSCAN based filtering method, showing the identification of distinct groups in (a), the calculation of cluster centroids in (b) and (c), and the filter determination in (d). Echoes flagged in (d) as filtered identify E-region echoes, noise identifies echoes classed as noise by DBSCAN, checked noise identifies echoes classed at noise that pass the check for a suitable cluster in the neighborhood, and min points identifies instances where insufficient data was available in a given 30-min window. The clustering technique demonstrates the filtering of coherent structures as a whole and minimizes the impact of non 1F echoes on the LE feature.

RUCK ET AL. 10 of 25

15427390, 2024, 9, Downloaded from https://agupubs

online library.wiley.com/doi/10.1029/2024SW003916, Wiley Online Library on [02/05/2025]. See the Terms and Conditions

articles are governed by the applicable Creative Commons License

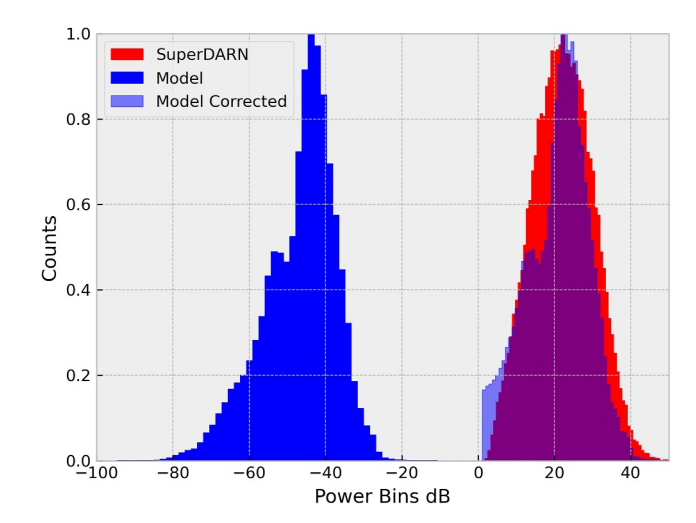


Figure 8. Power histograms for data in January 2014 for the Blackstone SuperDARN radar (red), the model (blue) and the normalized model with low power echoes removed (light blue). The normalization process shows good agreement between the corrected model and the Blackstone radar distributions.

2.3.4. Power Normalization

Issues arise when comparing the modeled and experimental power data, as whilst modeling the power distribution can be done reliably, the absolute values are more difficult to determine as noise must also be estimated due to SuperDARN power values being in terms of signal-to-noise ratio (SNR). These values are found by the SuperDARN FITACF procedure by fitting an exponential function to the envelope of a complex ACF and taking the value at zero-time lag as the power estimate.

To avoid complexities here, the power profile of the modeled data is normalized in relation to the power distribution peaks found by binning power into 75 bins across the range of each distribution. It should be noted that the log scales of modeled power and SuperDARN SNR values are different and are transformed here. Figure 8 shows the histograms for the two data sets for January 2014, with this corresponding to a power offset of 72.70 dB being applied to the data in this case. Simulation data contains rays that would exist below the receiver threshold of the radar, thus being undetectable and requiring removal prior to our comparison. To this end, simulation data with power values below the minimum power of the Blackstone radar power distribution are removed. This process is performed for each frequency band across each full month to avoid sudden changes in power at shorter timescales and to ensure sufficient data is available when creating the histograms.

3. Results

3.1. Example Backscatter Variation

To examine the capacity of the simulation to model the Blackstone radars' GS, the time evolution of backscatter echoes are plotted in Figure 9 for the 16th–18th January 2014. It should be noted that the local time is approximately 6 hr behind UTC for this specific radar. The LE of the GS is extracted by simply taking the minimum group range at each time step and is overlaid in black. Small-scale variations observed in the Blackstone radar GS at timescales below 1-hr resolutions are not captured within the simulation as the IRI offers only a smoothed representation of the monthly median ionosphere at a limited temporal resolution. The passage of TIDs is a known source of variability in daytime GS on timescales of approximately 1 hr (Samson et al., 1990) and is an example of a feature not within the modeled backscatter.

During the nighttime, almost no echoes are observed in both data sets. Upon inspection of Figure 2, it is clear that IS dominates at these time periods and so our analysis is limited to only daytime comparisons here. Good agreement is seen between the Blackstone radar and model LE at midday, with errors remaining within ± 250 km and large departures only occurring during the early morning. A notable offset in elevation angle is seen between the two, with the Blackstone radar consistently observing a higher elevation angle by approximately 10° .

Despite the GS LE showing good agreement, notable differences in the trailing edge distributions are seen. Despite the power corrections clearly reducing the extent of the model trailing edge, a significant overestimate remains. The same conclusion may be made for the long-range nighttime echoes seen in the model but not by the Blackstone radar. Both trailing edge and nighttime echoes occur at very low elevations that manifest in a significantly reduced power due to the falloff in gain at such elevations. Of course, the methods used to adjust the powers to be comparable is a considerable limitation here and so we must take any assessment of the power behavior with some measure of skepticism; as such, the absence of echoes in the Blackstone radar data, relative to the simulation, cannot necessarily be taken as indicative of a propagation difference. This reinforces the importance of utilizing the LE for comparisons due to the increase in observed power that occurs here.

3.2. Climatology

Investigation of model and Blackstone radar backscatter for several day periods is useful for assessment of errors during specific events, but is insufficient for validating general or long-term performance. We apply the modeling technique to the months of January and June in both 2014 and 2018 and present the LE characteristics in Figure 10

RUCK ET AL. 11 of 25

15427390, 2024, 9, Downloaded from https://agupubs. onlinelibrary.wiley.com/doi/10.1029/2024SW003916, Wiley Online Library on [02/05/2025]. See the Terms and Conditions (https://onlinelibrary.wiley.com/terms-and-conditions) on Wiley Online Library for rules of use; OA articles are governed by the applicable Creative Commons Licensea

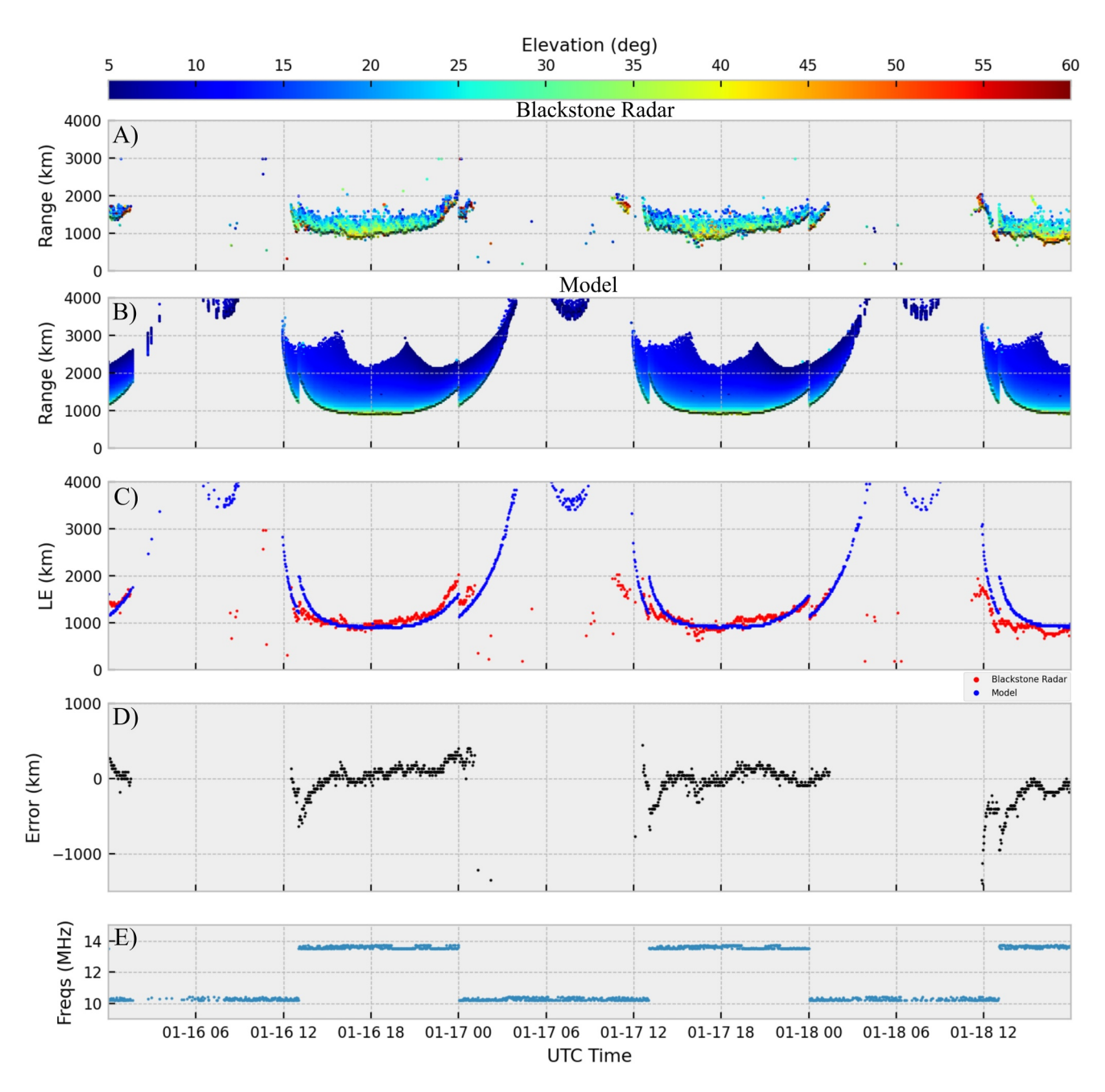


Figure 9. Variation in elevation angle for the Blackstone SuperDARN radar (a) and the model (b) between 16th and 18th January 2014. The leading-edge range is extracted and plot in (c) for Blackstone radar (red) and the model (blue). The error in leading edge range is included in (d) whilst transmission frequency is included in (e).

to capture the diurnal, seasonal and solar cycle climatology of errors. The variation in LE is binned down to 5-min intervals and averaged for this analysis. It is important to note that there is not full coverage of every bin across the months. This data sparsity is due to either the radar not being operational, a lack of GS, the filter removing non F-mode echoes, or significant absorption hindering detection. One should be careful to notice that the sudden step in LE at 13:00 UT in 2014 is due to the radar switching frequency and does not represent an immediate change in the ionosphere. This also occurs in 2018 but is not immediately visible as the difference between the day and night frequencies was much smaller.

The LE in both data sets shows the expected diurnal variations of retreating in the evening and returning in the morning, with the daytime LE also shown to occur at considerably closer ranges for winter compared to summer

RUCK ET AL. 12 of 25

15427990, 2024, 9, Downloaded from https://agupubs.onlinelibrary.wiley.com/doi/10.1029/2024SW003916, Wiley Online Library on [02/05/2025]. See the Terms and Conditions (https://onlinelibrary.wiley.com/terms-and-conditions) on Wiley Online Library for rules of use; OA articles are governed by the applicable Creative Corr

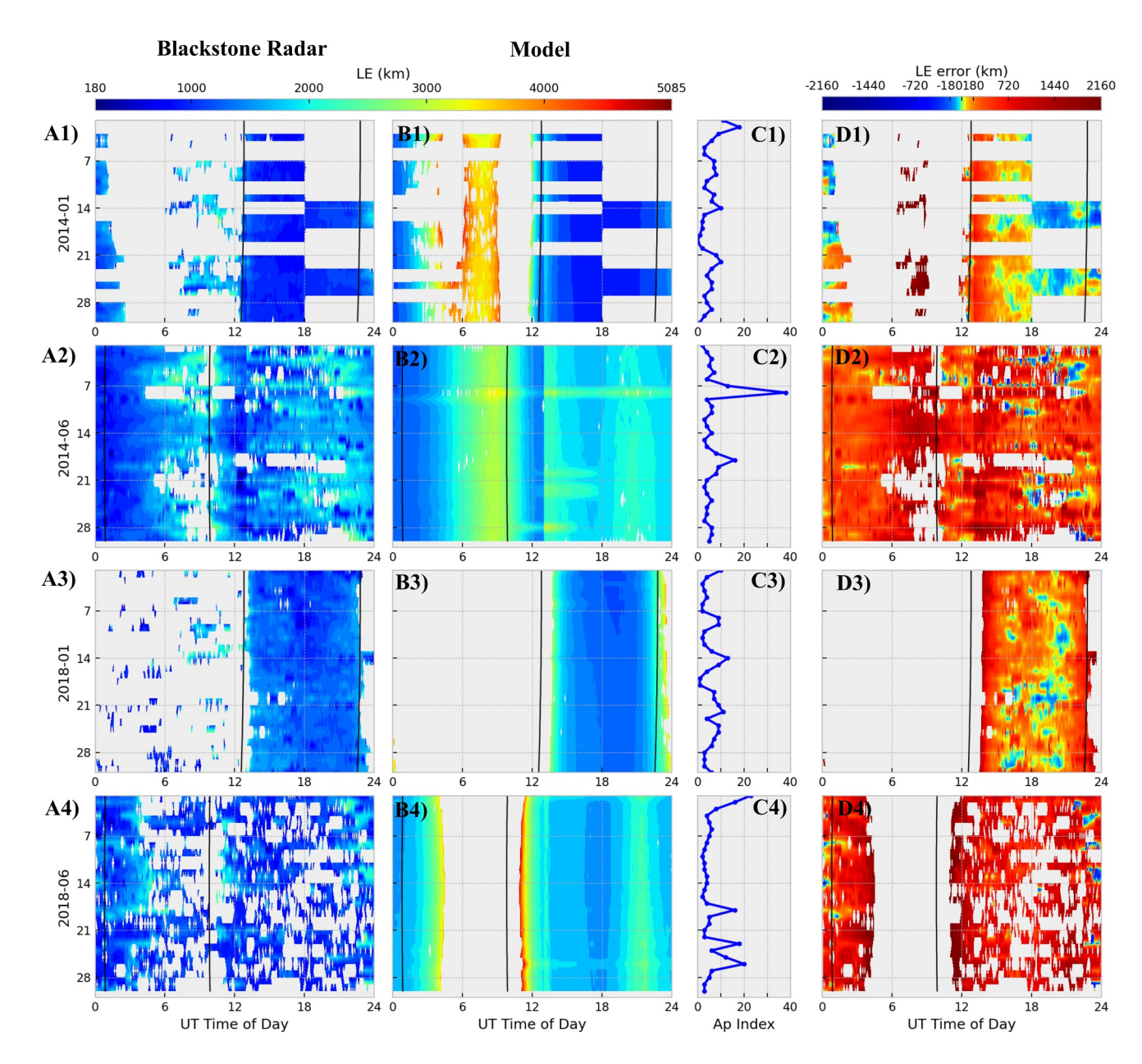


Figure 10. Variation of leading edge in January and June for both 2014 and 2018. Blackstone SuperDARN leading edge is provided in the first column, the model in the second, the Ap index in the third, and the calculated leading-edge errors in the fourth. One should note that leading edge errors are clipped to $\pm 2,160$ km to preserve dynamic range and in some rare cases, errors do exceed this. The error colormap is $\log 10$ scale and has contours every 45 km which corresponds to the group range resolution of the measurements. Data is not available for many periods in January 2014 and is the reason for large blocks of missing data. The time of the local solar terminator is shown by the black vertical lines for a point 500 km down range.

in both data sets as expected. This is due to the winter anomaly, a midlatitude phenomenon where unexpectedly high electron density values exceeding those in summer are observed during the winter daytime (Davies, 1965). As a result, higher elevation rays that correspond to closer ranges are supported through the relation in Equation 2 as suggested by Equation 1.

A geomagnetic storm occurs on 8th June 2014 as indicated by the Ap index and the increase in model LE. Unfortunately, echoes where not present within the Blackstone radar data for much of this day and is likely either due to increased ionospheric absorption coinciding with the storm or the negative ionospheric response causing the ionosphere to be unable to support propagation at the transmit frequency. Echoes that are present between 13:00–20:00 on this day indicate a consistent error exceeding 1,000 km throughout this period. The lack of data

RUCK ET AL. 13 of 25

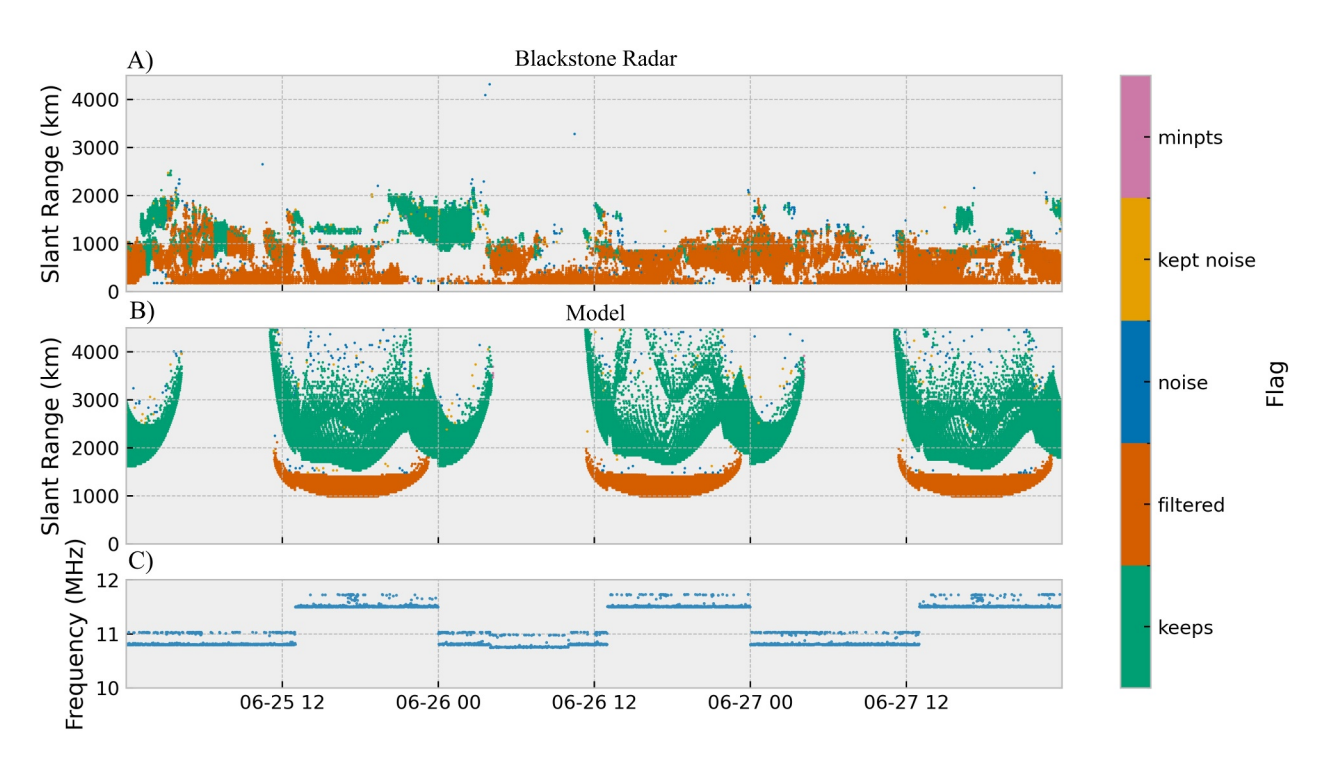


Figure 11. Example time variation of filter flags showing the presence of blanketing sporadic-E for much of June 2018. The filter performs reliably across this period, with minor inconsistencies where sporadic-E is incorrectly. The filtered echoes in the model are from 1E backscatter as sporadic-E is not modeled in the IRI2016 model. These echoes are likely also in the SuperDARN data but are difficult to distinguish from sporadic-E.

during this storm is a notable limitation of using these oblique HF measurements for validation and can likely only be mitigated by using multi-frequency soundings with greater transmit powers, such as in the backscatter sounders of OTHR systems. Recent work has been conducted by the SuperDARN community to include multi-frequency soundings.

Errors are seen to be most significant for all months at the time of the local terminator where LE ranges are increased and are generally lower during the middle of the day. Overall, LE errors are seen to be overestimates by the model with the exception of daytime LEs in January 2014. In January 2014, the ability of the model to fully capture the overall increasing LE following the month progression is demonstrated by daytime errors remaining below 500 km for the entire month.

The simulation predicts a population of nighttime echoes at extreme ranges of ~4,000 km not seen by the Blackstone radar in the month of January 2014, and this is attributed to low power echoes below the receiver threshold of the radar. Evidently, these have not been removed from the simulation during the power normalization process despite having expectedly high free space path losses and typically low antenna gain compared to the rest of the data. Nonetheless, periods where echoes occur in both the model and Blackstone radar LE are the focus of this validation and where errors are computed, as the absence of echoes is not necessarily indicative of the lack of propagation. One should be cautious about instances where sudden retreats in LE are seen in the Blackstone radar data as this is not conclusive of a physical change in the ionosphere but may be caused by limitations in the data or filtering. This can be seen at 22:00 on the 4th June 2018 and is likely non-physical as Sporadic-E is prevalent during this period and can prove difficult for the filter. We do not consider this to be a significant limitation as this is expected from this data and impacts a relatively insignificant proportion of the overall data.

The presence of a sporadic-E layer blanketing 1F echoes is a noticeable effect in the summer months, especially in 2018. Here, the cluster filter essentially removes all echoes as the regular occurrence of sporadic-E is either the sole source of echoes, or where 1F is not entirely blanketed, it often forms a cluster that cannot be fully separated from the 1Es-mode and so both are removed. This is a fortunate effect of the filter, as for periods where a LE cannot be suitably extracted, all data is typically removed due to the low centroid range and virtual height. This largely prevents comparison of otherwise uncertain data. A summary plot of a period where Sporadic-E is significant is presented in Figure 11, showing the capacity of the filter to reliably remove almost all of the unwanted

RUCK ET AL. 14 of 25

15427390, 2024, 9, Downloaded from https://agupubs.onlinelibrary.wiley.com/doi/10.10292024\$W003916, Wiley Online Library on [02/05/2025]. See the Terms and Conditions (https://onlinelibrary.wiley.com/doi/10.10292024\$W003916, Wiley Online Library on [02/05/2025]. See the Terms and Conditions (https://onlinelibrary.wiley.com/doi/10.10292024\$W003916, Wiley Online Library on [02/05/2025]. See the Terms and Conditions (https://onlinelibrary.wiley.com/doi/10.10292024\$W003916, Wiley Online Library on [02/05/2025]. See the Terms and Conditions (https://onlinelibrary.wiley.com/doi/10.10292024\$W003916, Wiley Online Library on [02/05/2025].

erms-and-conditions) on Wiley Online Library for rules of use; OA articles are governed by the applicable Creative Commons Licenso

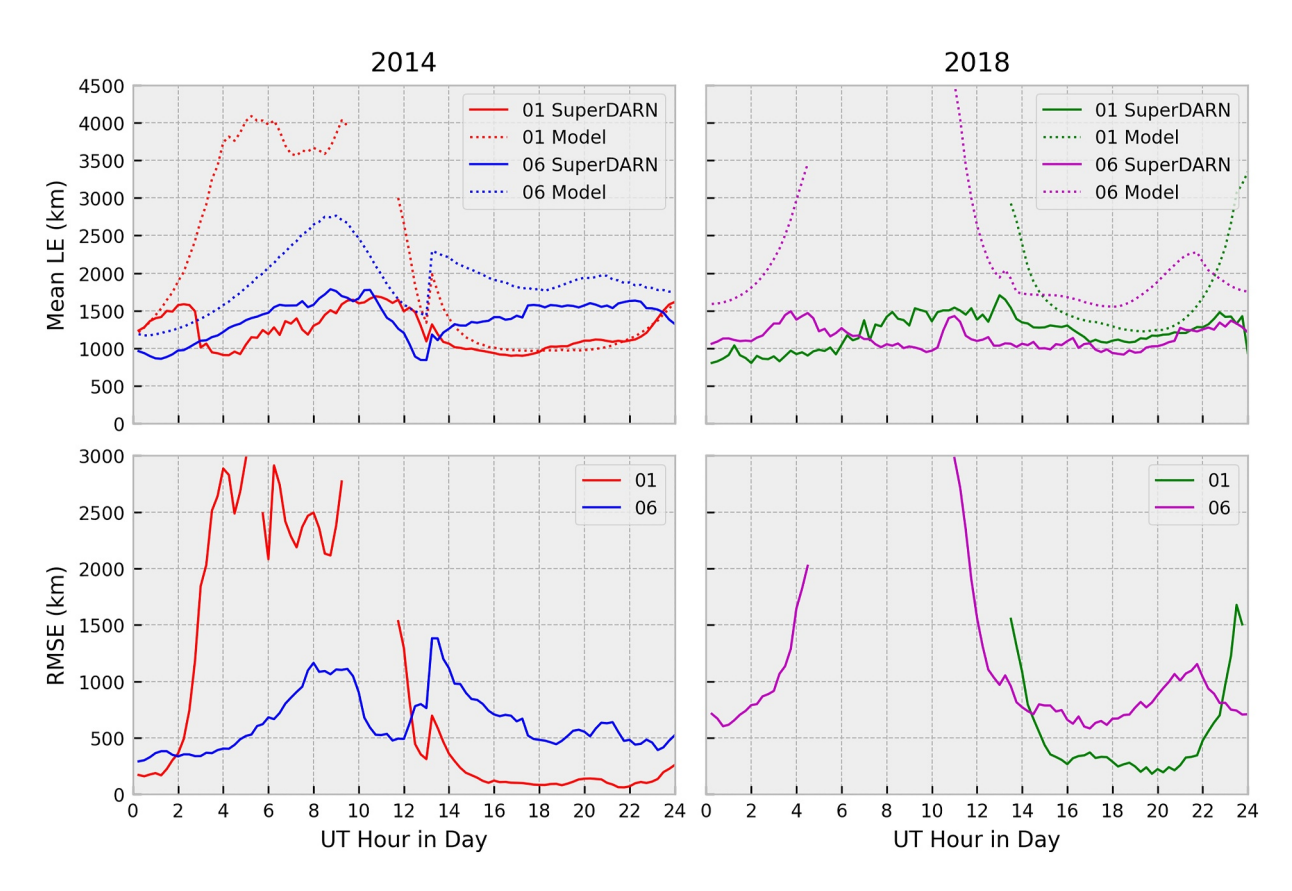


Figure 12. Day variations in 15-min month averaged leading edge slant range (top) and the corresponding RMSE (bottom) in 2014 (left) and 2018 (right). Instances where no data is available restricts full day coverage of this analysis in all cases but June 2014. The local time at this radar approximately is approximately 6 hr behind UTC.

echoes, whilst keeping what 1F-mode can be reliably identified. It should be noted that there are clear instances in Figure 11 where the filter does not correctly remove non-1F echoes such as at approximately 03:00 and 08:00 on the 25th.

A more concise assessment of LE error climatology can be facilitated by averaging across the month in the form of a 15-minutely RMSE as presented in Figure 12. The monthly averaged performance of the model during the daytime is seen to be reasonable, showing errors as low as 100 and 250 km for January 2014 and 2018, respectively. For this context, 100 km is considered a low level of error as the group range resolution of the Blackstone radar is 45 km and we often see minute-to-minute variability of the leading edge across 2–3 range bins such as in Figure 9. In contrast, positioning errors for OTHR are typically expected to be less than 30 km in range and measurement resolution is approximately 3–30 km for normal operating modes (Fabrizio, 2013).

It is reassuring to observe stable performance across the daytime hours in January of each year, as this suggests we can expect acceptable accuracy when modeling oblique propagation using the IRI-2016 model at these times. Despite this, summer performance is seen to be degraded, showing minimum errors of 400 km and significant departures approaching 800 km, albeit this may be partially attributed to nuisance Sporadic-E degrading the data quality. In Figure 12, caution is recommended when inspecting periods of data sparsity, as this will degrade the robustness of our statistical analysis. To this end, nighttime LE assessments in January 2014 and the full month of June 2018 are generally less reliable due to the absence of consistent data. Errors in the nighttime hours exceed 1000 km in all months.

3.3. Elevation Angle Distributions With Group Range

The provision of elevation data by the SuperDARN interferometers permits further inspection of model errors beyond the LE analysis, as we can directly compare the slant range-elevation distributions between the two data sets. This comparison is presented in Figure 13 for three UT times, where the 2D histograms are created by

RUCK ET AL. 15 of 25

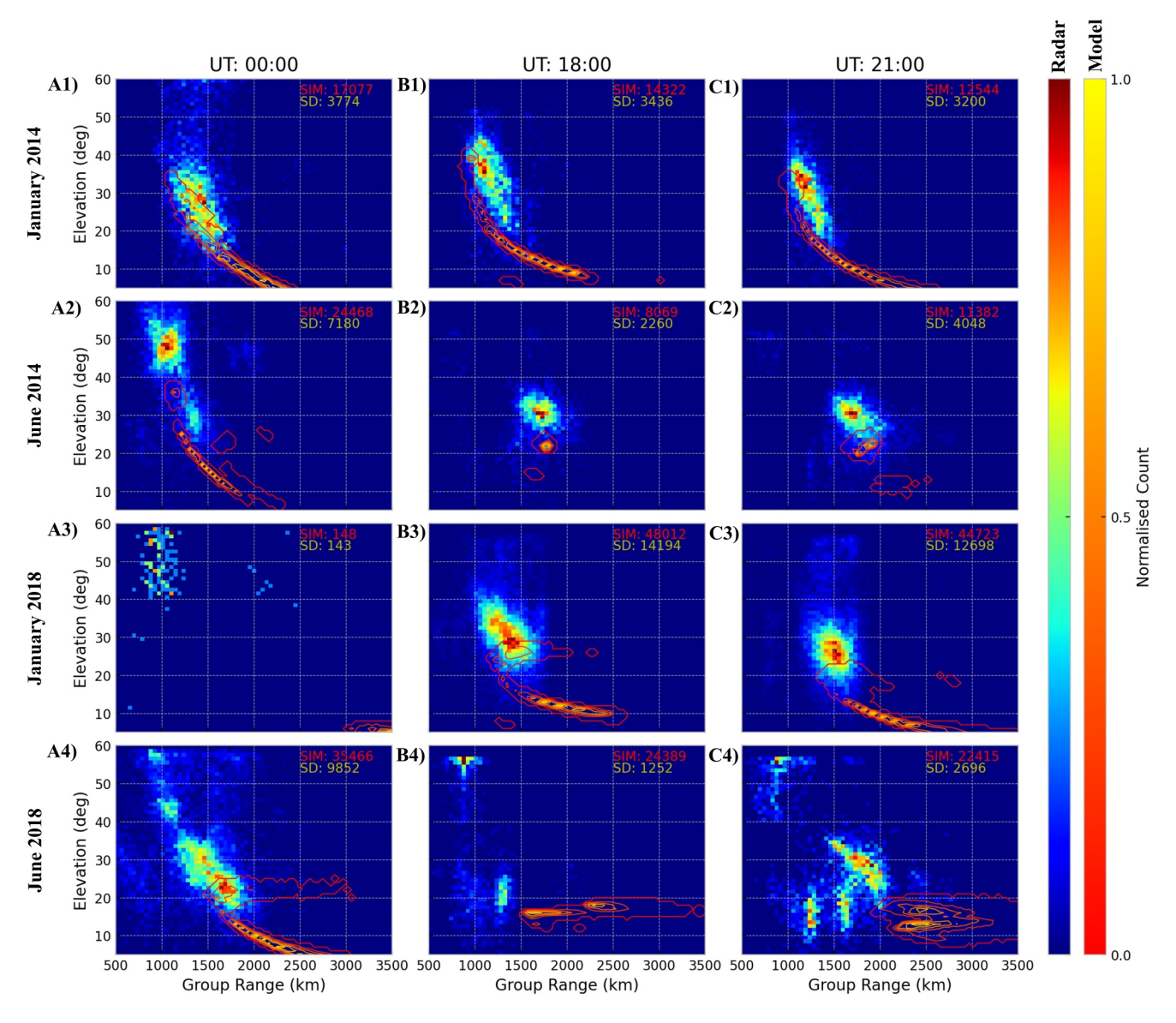


Figure 13. Slant range - elevation echo distribution histograms for the Blackstone radar shown by the base colormap and for the model by the overlayed contours. All echoes occurring within the specified hour across the full month are included in each panel, with the total count included indicated in the top right corner of each.

including all echoes across the month occurring within the specified hour for 1° elevation bins. As these distributions are averaged across the full month, we see a much greater broadening of the Blackstone radar echo distributions as compared to the simulation due to the greater variability of the real ionosphere in comparison to the monthly median IRI-2016. The merit of elevation angle estimates within SuperDARN data is notable in this context, as the upper limit to echo elevation values that are physically possible is directly related to NmF2 to the first order by Equation 2. It is important to note that whilst Equation 2 can provide useful context when diagnosing errors in NmF2, an equation that incorporates spherical Earth geometry such as in (Gillies et al., 2009) should be used when calculating absolute NmF2 error values. Figure 14 permits diagnosis of potential NmF2 and hmF2 errors whilst highlighting distinct propagation modes so that the effectiveness of the E-region filter can be assessed.

Figure 13 shows generally good agreement between the Blackstone radar and model distribution LEs in January 2014, where the average LE is seen to occur between 1,000- and 1,300-km with the closest range occurring near the middle of the day at 18:00 UT as expected. At high elevations, the distributions occupy the same range-

RUCK ET AL. 16 of 25

15427390, 2024, 9, Downloaded from https://agupubs. onlinelibrary.wiley.com/doi/10.1029/2024SW003916, Wiley Online Library on [02/05/2025]. See the Terms and Conditions (https://onlinelibrary.wiley.com/terms-and-conditions) on Wiley Online Library for rules of use; OA articles are governed by the applicable Creative Commons Licensea

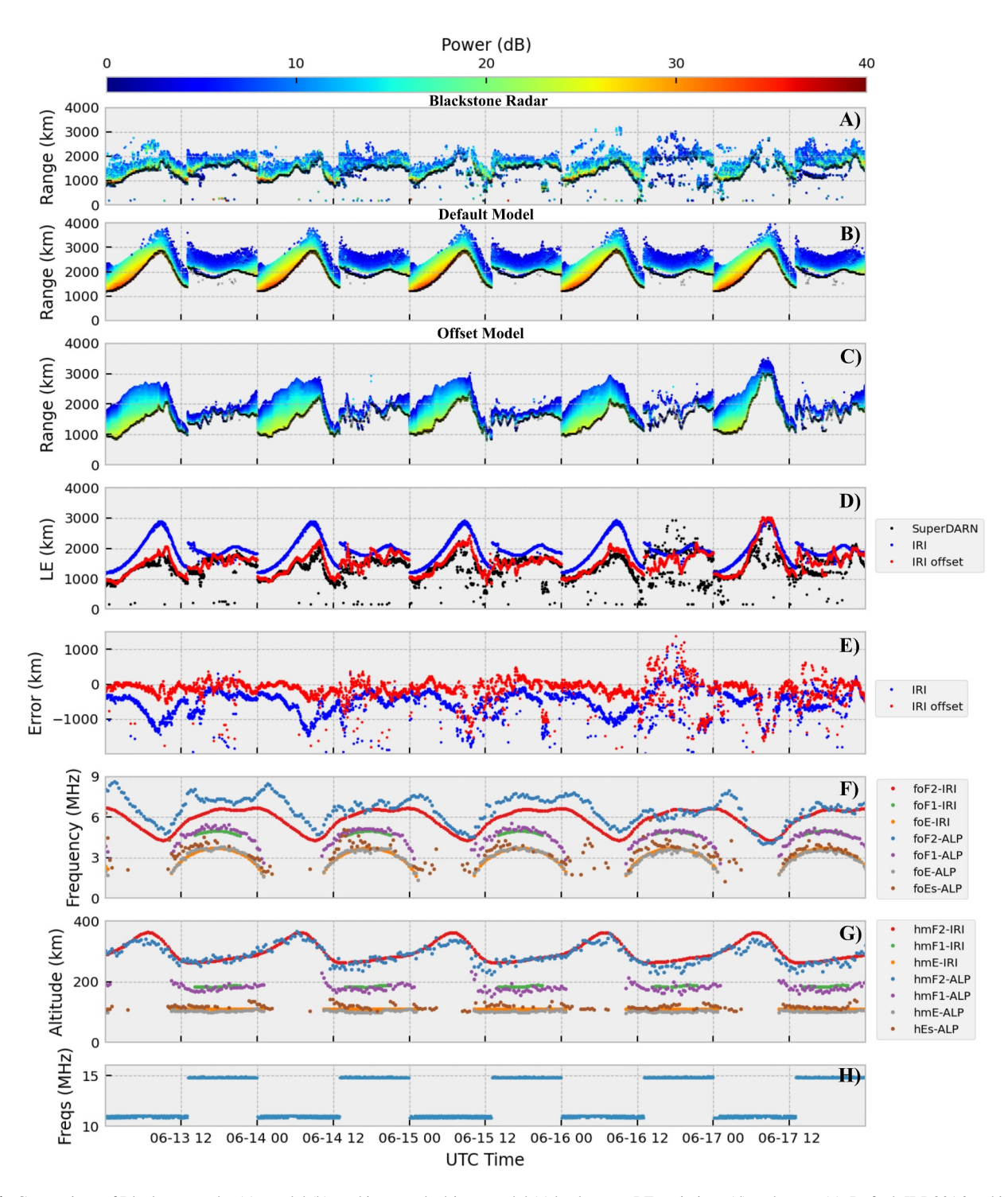


Figure 14. Comparison of Blackstone radar (a), model (b), and ionosonde driven model (c) backscatter LE variations (d) and errors (e). Default IRI-2016 and ionosonde peak density and height parameters are compared in panels (f) and (g), respectively, whilst operating frequency is provided in (h).

elevation space for this month but begin to depart at lower elevations as the Blackstone radar trailing edge does not extend in the same manner. As previously mentioned, this is likely due to low power echoes not being detected; however, it is important to note that this results in the peak of the model contour shifting toward further ranges and lower elevations. This is also seen to occur at 00:00 in June 2014, 18:00 and 21:00 UT in January 2018 and in all of June 2018, suggesting a systematic overestimate of trailing edge power.

RUCK ET AL. 17 of 25

At 18:00 and 21:00 UT of June 2014, we see distinct localized peaks in the distributions, with minimal spread in elevation for both Blackstone radar and model data, indicating that the model predicts this behavior well. Nonetheless, we observe a distinct offset in the elevation peaks of approximately 8° that suggests the model is likely underestimating NmF2 here. A similar difference was observed by Oinats et al. (2016) and was attributed to underestimates in the IRI's representation of the electron density peaks. An interesting number of echo populations are observed at 00:00 UT of June 2014 that suggests distinct propagation modes. Whilst the low-density group centred on 47° at 1,900 km is a distinct contribution from 2F echoes, the two closer peaks appear to both be 1F echoes. The occurrence of a double peak population can be explained by variability in the ionospheric peak density broadening the distribution, and inspection of the processed data confirms this as no E-region echoes are observed

Insufficient data is available for 00:00 Jan 2018 due to the lack of nighttime echoes. Conversely, the distributions at 18:00 and 21:00 show the greatest number of echoes that permits underestimates in elevation to be identified for these times

The presence of Sporadic-E is clearly identifiable during June 2018 by the characteristically high elevation angles occupied by these distributions at close ranges. We also see a distinct E-mode population at 15° at a range of 1,250 km at 21:00 UT at closer ranges than expected for the 1F population. Whilst it is clear the filter has accepted a statistically significant number of E-region echoes, it is reassuring that the 1F echoes are presented so dominantly at 00:00 and 21:00 and that any were recovered from this period. However, it is insufficient to warrant a reliable analysis of the LE due to the statistical significance of E-region echoes in the data.

An interesting feature observed in the model for 00:00 of June 2014, 18:00 and 21:00 of January 2014 and in June 2014 is that of a broadening of the distribution at higher elevations toward further ranges in the shape of a "C." This is characteristic of high angle rays occurring within the F-region and are typically associated with low powers due to the defocusing effect of rays near the F-layer peak.

3.4. Ionosonde Conjunction

To demonstrate the potential performance of the model when ionospheric peak parameters are known, we simulate the period of 13th-17th of June 2014 with the IRI-2016 model driven by ionosonde measured values. The Alpena ionosonde located down range of the radar at 45.1 N, 83.6 W is used in this assessment and provides an opportunity to assess the robustness of our validation technique. These results are presented in Figure 14 and are compared to that of the default model for context. Ionograms recorded at 15-min intervals throughout this period are manually scaled to extract ionospheric parameters and presented in comparison to model values in panels F and G of Figure 14. As the IRI-2016 model permits the manual input of any of the bottomside parameterization values, we take the relative difference between the ionosonde and IRI-2016 parameters at the nearest point on the radar beams great circle (GC) path and apply constant multipliers to the entire GC slice such that the parameters match exactly at that point. The offset location is 45.24 N, 83.51 W and corresponds to a ground range of 1,016.7 km from the radar and 16.7 km from the ionosonde. At times when the IRI-2016's F1 region model is inactive, it is not possible to override the parameter, and so we are forced to leave it off, which is at times in disagreement with the ionosonde. Whilst the ionogram measurements are only representative of the ionosphere for an area related to the typical ionospheric decorrelation distance (Forsythe et al., 2020), they provide a useful means to assess modeled ionospheric dynamics beyond the monthly median. This is clear by the introduction of traveling ionospheric disturbance (TID) features into the modeled backscatter in Figure 14 panel (c), which are not seen in the default IRI-2016 in panel (b).

It is immediately clear upon inspection of Figure 14 that the ionosonde input provides a dramatic improvement in both the modeled backscatter echo distribution and LE variation, with the latter showing errors centred near zero for much of the period and at times providing improvements in excess of ~800 km. The greatest improvements are regularly seen during the nighttime periods. Panel (f) shows that almost all of this improvement can be attributed to the mitigation of errors in NmF2, as the IRI-2016 is otherwise able to represent all other parameters with reasonable accuracy, except for the occurrence of the F1 region and of course the presence of sporadic-E.

A clear limitation in our approach here is that minor TID features measured by the ionosonde and seen in the Blackstone radar data are massively overestimated. This is likely because such features are often localized over a

RUCK ET AL. 18 of 25

15427990, 2024, 9, Downloaded from https://agupubs.onlinelibrary.wiley.com/doi/10.1029/2024SW003916, Wiley Online Library on [02/05/2025]. See the Terms and Conditions (https://onlinelibrary.wiley.com/terms-and-conditions) on Wiley Online Library for rules of use; OA articles are governed by the applicable Creative Commons Licensea

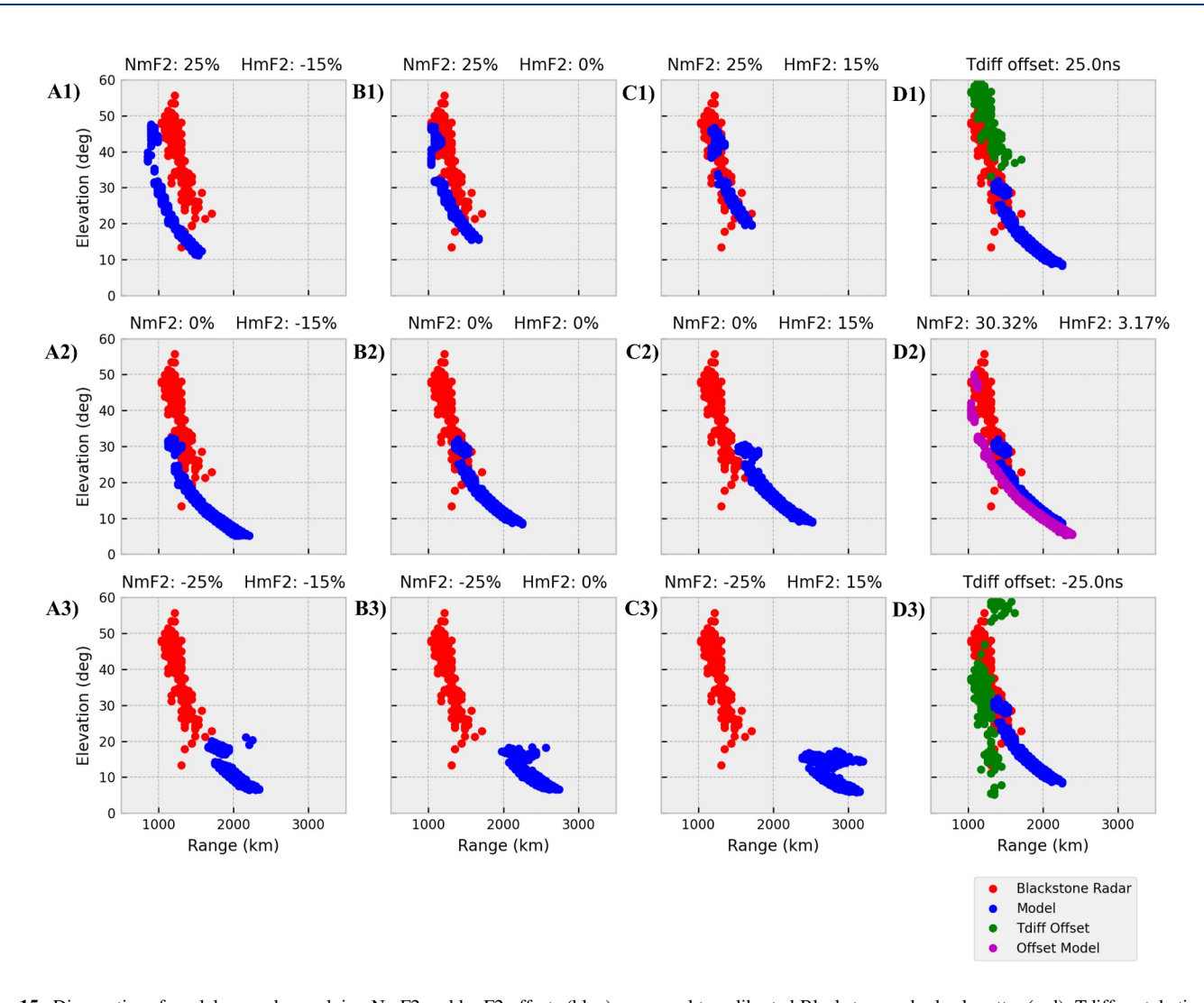


Figure 15. Diagnostics of model errors by applying NmF2 and hmF2 offsets (blue) compared to calibrated Blackstone radar backscatter (red). Tdiff pertubations are demonstrated in panels (D1) and (D3) in (green), with ionosonde driven model backscatter also shown in (D2) in (magenta).

relatively small distance and are inherently directional; this presents problems in our model as the ionosonde is not directly under the reflection point and our offsets are applied equally along the GC.

A small number of echoes are present at 9:00 UT on the 15th and 17th and cause a significant increase in errors for both modeled LEs, with these appearing to be either auroral E-mode or ½-hop echoes that are not properly removed by the filtering or ground flag, respectively. It is unexpected to see echoes at such close ranges during the night time as 1F echoes are typically seen to retreat to further ranges as the ionospheric density drops and only low elevation angles are available. Furthermore, E-mode echoes remain in the Blackstone radar data at 21:00 UT on the 15th and at 22:00 on the 16th, with this corresponding to an unreasonable increase in both modeled LE's. It is interesting to note however, that a small population of echoes is often seen in all three data sets ahead of the main 1F backscatter during several of the days that arises from the F1-region. The occurrence of this feature coincides with increased errors and error spread in the modeled LE's as the small population appears inconsistent in both the Blackstone radar and driven model data, potentially being due to such low echo powers as suggested by Figure 14. Nonetheless, Figure 14 demonstrates that improvements in model NmF2 values can dramatically improve model performance such that the much of the real propagation environment can be reliably modeled using numerical raytracing.

3.5. Error Diagnostics

Significant insights can be gained on the origin of model errors by exploring the effect of offsets to model NmF2 and hmF2, specifically how these parameters impact the range elevation distribution of echoes. To examine the

RUCK ET AL. 19 of 25

impact of specific errors in the ionospheric model on the range-elevation space, we simulate the hour of 3:00 on the 14th of June 2014 with combinations of $\pm 25\%$ and $\pm 15\%$ offsets to NmF2 and hmF2, respectively. Furthermore, we recalculate elevation angles for the Blackstone radar data in panel D1 and D3 with ± 25.0 ns offsets from the calibrated values of $T_{\rm diff}$. This seeks to demonstrate the relative impact of the ionosphere and interferometry on the distributions and to present the effect of uncalibrated $T_{\rm diff}$ values on the error analysis.

From Figure 15 it is clear that an increase in NmF2 shifts the distribution forward and up to higher elevations, with the opposite being true for a negative offset. Conversely, modifying hmF2 does not impact the elevations occupied by the distribution and instead a forward and backwards translation in slant range is seen for negative and positive offsets, respectively. We see that the applied offsets account for deviations in elevation and range of approximately 15° and 300 km in each direction, respectively. Besides hmF2 modifications resulting in range translations, we also see a minor shift in elevation angles. This is an expected result and is due to changes in NmF2 that arise as the location of the reflection point is shifted in range to a different region of the downrange ionosphere.

By the apparent difference between the original model (B2) and that of the model offset by +25% NmF2 (B1) demonstrating a much better agreement with the Blackstone radar distribution, we can infer that there is an error in NmF2 on the order of 30%. This is in direct agreement with the ionosonde driven distribution (D2) that confirms that the difference in the modeled and measured NmF2 values differ by 30.32% and show better agreement with the Blackstone radar distribution with this offset applied.

As noted by Ponomarenko et al. (2018), the relation between measured phase and elevation angle is highly nonlinear, and this is demonstrated by the distribution occupying a significantly greater range of elevations in panel D3 as opposed to that in D1. The range of elevations occupied by the echoes is dramatically changed by the $T_{\rm diff}$ offset, with a +25 ns offset having elevations covering 30°-60° and the -25 ns offset having a much broader range of 5°-60°. The deviation in elevation near the top of the distributions for the $T_{\rm diff}$ offsets is approximately 5° from the calibrated value, and this remains relevant when compared to the impact of NmF2 offsets. Thus, when diagnosing NmF2 information from SuperDARN elevation data, it is paramount that the data is properly calibrated.

4. Discussion

The marked increase in errors at times near the local terminator seen in our analysis for Figures 9, 10, 12 and 13 is expected. These periods present a marked challenge that some ionospheric models may perform poorly during the rapidly changing NmF2 and hmF2, meaning incorrect timings of sunrise or sunset by the model can result in large errors in these values. A further expected shortcoming for the IRI at these periods is its inclusion of an occurrence based F1-layer that toggles on and off abruptly as this can introduce non-physical density gradients along the generated great circle grid. Despite this, our method identifies that the model performs poorly during these periods as we would expect, indicating that caution is warranted when performing HF modeling with the IRI near the terminator.

Whilst our technique may be applied to any radar in the network, further caution is required when using radars with the LPDA array due to the requirement to use the FOV detection algorithm. Despite the algorithm providing reliable classification of most echoes, the impact of unassigned echoes thinning the data can hinder a robust analysis. In the case that LE echoes are unassigned, the LE will appear further in range and may suggest either errors in the model or an improved agreement; both of which may not be true. This is a notable limitation of our method, and it is hoped that improvements can be achieved through optimisation of the FOV algorithm parameters.

In all backscatter simulated by the model, a considerable overestimate of the trailing edge extent has been noted and attributed to the power normalization technique included herein. Beyond limitations in the approach, the problem is likely related to the quality of the default D-region model in the IRI-2016 resulting in incorrect absorption estimates. Future comparison of the IRI-2016 model with a different D-region model, such as that from the Faraday International Reference Ionosphere (FIRI) (Friedrich et al., 2018), will provide evidence on the origin of the trailing edge overestimate. Better agreement with SuperDARN backscatter in this case will support the normalization technique and demonstrate that the inconsistency is representative of the model description.

RUCK ET AL. 20 of 25

However, further investigation in this area is required. We therefore restrict our current analysis of the trailing edge as it is not necessarily indicative of the model.

The formation of Sporadic-E layers at midlatitudes is a significant issue for HF radars operating in these regions during the summertime when Sporadic-E, caused by convergence by diurnal and semi-diurnal tides (Haldoupis, 2012; Hodos et al., 2022; Kunduri et al., 2023), is quite common as these formations can significantly degrade the performance of such radars by limiting the maximum ranges that can be reached. Plasma comprising Sporadic-E layers is often of sufficiently high density that it is capable of blanketing propagation to higher regions of the ionosphere by reflecting HF radio waves at a wide range of elevation angles in this lower region. As our current focus is on assessments of the 1F echo variations, we see this as a significant limitation for the Super-DARN data, which limits our current analysis to periods where Sporadic-E is not present. The blanketing effect of Sporadic-E is a phenomenon that limits validation using any ground-based HF instruments. Besides not entirely blocking the F-region, auroral-E echoes are also observed in some of the data and indicate a further source of ionisation that can present significant departures between the modeled propagation with that of the real ionosphere. We have previously demonstrated the sensitivity of OTHR coverage and propagation with aurora, including the occurrence of ducted modes (Ruck & Themens, 2021).

This raises the important question of whether errors calculated for models where E-region echoes such as Sporadic-E, auroral-E, and meteor scatter are not removed is a more thorough validation; we follow the opinion that whilst this would result in the truest validation, it serves little purpose beyond degrading the usefulness of such comparisons for ionospheric models that do not contain deliberate considerations to these features. The problem of Sporadic-E we experience in the Blackstone radar data, and our removal efforts highlights the significant impact of not including these ionisation features in models. It is also important to note that whilst we remove E-region echoes in our comparisons, it is obvious that the actual ionisation in the real ionosphere remains and will have an impact on the cumulative path of propagating radio waves reflected by the F-region.

Although E-region echoes present a challenge for our current analysis, we see notable success with our cluster-based filtering approach in this task, which may be applicable to studies focussed on the automatic detection of Sporadic-E and auroral-E in the context of climatological assessments. We observed Sporadic-E to occur for a considerable proportion of the summer months we investigate here with substantial modifications to the propagation environment seen. To this end, the performance of operational systems without inclusion of Sporadic-E models is expected to be catastrophic for midlatitude OTHR, particularly for the FMS where the notable modifications to available ranges manifest as incorrect coverage predictions with errors in excess of 1,000 km. Furthermore, the same problem applies to Arctic OTHR operating within the vicinity of the aurora (Ruck & Themens, 2021). It is these considerations that motivate the development of regional ionospheric models such as that of the Empirical Canadian High Arctic Ionospheric Model (E-CHAIM) (Themens et al., 2017, 2018, 2019; Watson et al., 2021) or Global Positioning System Ionospheric Inversion (Fridman et al., 2006, 2009) that can represent a greater proportion of the features observed in the regional ionosphere.

Due to the significant information that can be gained from assessment of the SuperDARN range-elevation distributions on NmF2 and hmF2, we envision this data set as being highly suitable for validation or assimilation into RTIMs. Such use demands that a reliable means of interferometer calibration monitoring can be performed in real time using an automated technique such as that by Ponomarenko et al. (2018). This is required to ensure significant non-physical changes in elevation angle are detected and not included into the assimilation. In this work we have not considered the impact of thickness parameters on the range-elevation distributions and the information that may be ascertained. It is expected that the use of ionospheric models utilizing data assimilation schemes will show much reduced errors in LE due to their better representation of the immediate ionosphere.

5. Conclusions

We have demonstrated a new technique for performing validation of ionospheric models using the SuperDARN ground backscatter data set. Our method has shown utility in assessing model errors at a range of timescales for propagation contextually relevant for OTHR operation. The LE based assessment provides a contextualization of what positional accuracy we may expect in OTHR coordinate registration and how this may vary through time for a given model. We show that analysis of range-elevation distributions permits significant information to be gleaned on the origin of model errors with good agreement with ionosonde values. Beyond this, we provide context to the extent of elevation calibration errors on the echo distributions and show they can be significant in

RUCK ET AL. 21 of 25

15427390, 2024. 9, Downloaded from https://agupubs.onlinelibrary.wiley.com/doi/10.1029/2024SW003916, Wiley Online Library on [02/05/2025]. See the Terms and Conditions (https://onlinelibrary.wiley.com/terms-and-conditions) on Wiley Online Library for rules of use; OA articles are governed by the applicable Creative Comm

the context of NmF2 errors. The demonstration of ionosonde driven model backscatter conclusively shows that model performance can be dramatically improved by better representations of NmF2, with improvements of ~800 km observed during the nighttime. For the IRI-2016 model, we observed monthly averaged RMS leading edge errors consistently below 400 km during the daytime hours of January 2014 and 2018, with significant increases during the nighttime and as the terminator approaches. Overall model performance was seen to be considerably worse during summer, with this attributed to the addition of more propagation modes and blanketing Sporadic-E degrading our data. We note the critical importance of including Sporadic-E in operational models for midlatitude systems as it is expected to be catastrophic for HF radar operation if not appropriately considered. Based on our current analysis of IRI-2016 performance at Blackstone, we believe this method provides a distinct opportunity to perform quantitative validation campaigns of models over a wide range of geographical areas and time periods by expanding analysis to other radars in the network.

Appendix A: Internal HFRM Profiles and TDIFF Calibration Values

Figure A1 shows the neutral temperature and density profiles used internally within HFRM as part of the ionospheric absorption calculation.

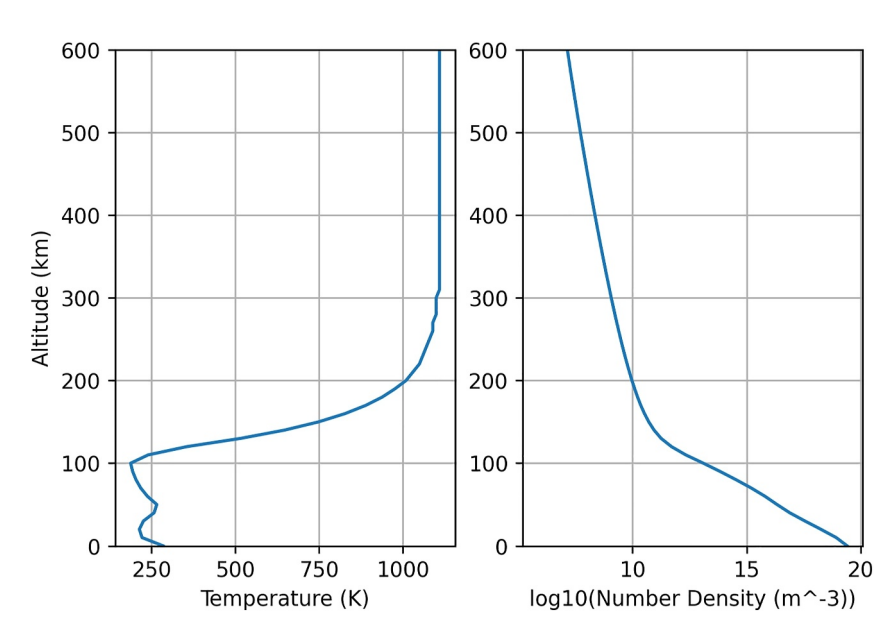


Figure A1. Neutral atmosphere temperature and number density profiles used to calculate ionospheric absorption.

The interferometer calibration values of T_{diff} used in this study are provided in Table A1.

 Table A1

 Interferometer Calibration Values for Each Month of the Validation Period

$T_{\rm diff}$ (ms)	2014	2018
January	-0.322	-0.330
June	-0.332	-0.327

Note. During periods of high noise during January 2014, an alternate value of -0.320 ms is used. This data is also available in the Data Availability section.

Data Availability Statement

Antenna radiation patterns modelled and used in this validation study are available for access and download from (Ruck, 2024a). All validation data produced in this study for figures and analysis is available for access and download from (Ruck, 2024b). The International Reference Ionosphere (IRI) model is available from the

RUCK ET AL. 22 of 25

15427390, 2024, 9, Downloaded from https://agupubs

onlinelibrary.wiley.com/doi/10.1029/2024\$W003916, Wiley Online Library on [02/05/2025]. See the Terms and Conditions (https://onlinelibrary.wiley.com/

following website https://irimodel.org/. The High Frequency Radar Model (HFRM) used to model propagation is the proprietary property of the Space Environment and Radio Engineering (SERENE) group at the University of Birmingham and is not available for public distribution to the research community. For access to HFRM, researchers should contact the lead author.

Acknowledgments

The SuperDARN data used in this study was accessed through the University of Saskatchewan's SuperDARN data repository. Raw SuperDARN data used in this study together with the licensing information and data description are available from Federated Research Data Repository (FRDR), Canada, at (Super Dual Auroral Radar Network, 2021a, 2021b). The RAWACF data can be read and processed using the Radar Software Toolkit (RST) written in C (SuperDARN Data Analysis Working Group, 2022). The Blackstone SuperDARN radar is maintained and operated by Virginia Tech under support by NSF Grant AGS-1935110. We acknowledge the use of SuperDARN data. SuperDARN is a network of radars funded by national scientific funding agencies of Australia, Canada, China, France, Italy, Japan, Norway, South Africa, the United Kingdom, and the United States of America. We are very grateful to these groups for their support of this work and their continuing provision and maintenance of this data. This work is supported in part by Canadian Space Agency Grant 21SUSTCHAI and the United States Office of Naval Research via its PRISM programme. PP is supported by GO Canada Grant G00024607 from the Canadian Space Agency. AGS is supported by the Office of Naval Research.

References

- Bland, E. C., McDonald, A. J., de Larquier, S., & Devlin, J. C. (2014). Determination of ionospheric parameters in real time using SuperDARN HF Radars. *Journal of Geophysical Research: Space Physics*, 119(7), 5830–5846. https://doi.org/10.1002/2014JA020076
- Bristow, W. A., Greenwald, R. A., & Samson, J. C. (1994). Identification of high-latitude acoustic gravity wave sources using the Goose Bay HF Radar. *Journal of Geophysical Research*, 99(A1), 319–331. https://doi.org/10.1029/93JA01470
- Burke, G. J., & Poggio, A. J. (1981). Numerical Electromagnetics Code (NEC) method of moments. Part 1: Program description theory. Retrieved from http://www.nec2.org/other/nec2prt1.pdf
- Burrell, A. G., Milan, S. E., Perry, G. W., Yeoman, T. K., & Lester, M. (2015). Automatically determining the origin direction and propagation mode of high-frequency radar backscatter. *Radio Science*, 50(12), 1225–1245. https://doi.org/10.1002/2015RS005808
- Chakraborty, S., Ruohoniemi, J. M., Baker, J. B. H., & Nishitani, N. (2018). Characterization of short-wave fadeout seen in daytime SuperDARN ground scatter observations. *Radio Science*, 53(4), 472–484. https://doi.org/10.1002/2017RS006488
- Chen, J., Ren, X., Zhang, X., Zhang, J., & Huang, L. (2020). Assessment and validation of three ionospheric models (IRI-2016, NeQuick2, and IGS-GIM) from 2002 to 2018. *Space Weather*, 18(6), e2019SW002422. https://doi.org/10.1029/2019SW002422
- Chisham, G., Burrell, A. G., Marchaudon, A., Shepherd, S. G., Thomas, E. G., & Ponomarenko, P. (2021). Comparison of interferometer calibration techniques for improved SuperDARN elevation angles. *Polar Science*, 28, 100638. https://doi.org/10.1016/j.polar.2021.100638
- Chisham, G., Lester, M., Milan, S. E., Freeman, M. P., Bristow, W. A., Grocott, A., et al. (2007). A decade of the super dual auroral radar network (SuperDARN): Scientific achievements, new techniques and future directions. Surveys in Geophysics, 28(1), 33–109. https://doi.org/10.1007/s10712-007-9017-8
- Chisham, G., Yeoman, T. K., & Sofko, G. J. (2008). Mapping ionospheric backscatter measured by the SuperDARN HF radars Part 1: A new empirical virtual height model. *Annales Geophysicae*, 26(4), 823–841. https://doi.org/10.5194/angeo-26-823-2008
- Chou, M.-Y., Yue, J., Wang, J., Huba, J. D., El Alaoui, M., Kuznetsova, M. M., et al. (2023). Validation of ionospheric modeled TEC in the equatorial ionosphere during the 2013 March and 2021 November geomagnetic storms. *Space Weather*, 21(6), e2023SW003480. https://doi.org/10.1029/2023SW003480
- Coleman, C. J. (1997). On the simulation of backscatter ionograms. Journal of Atmospheric and Solar-Terrestrial Physics, 59(16), 2089–2099. https://doi.org/10.1016/S1364-6826(97)00038-2
- Coleman, C. J. (1998). A ray tracing formulation and its application to some problems in over-the-horizon radar. *Radio Science*, 33(4), 1187–1197. https://doi.org/10.1029/98RS01523
- Custovic, E., Nguyen, H. Q., Devlin, J. C., Whittington, J., Elton, D., Console, A., et al. (2011). Evolution of the SuperDARN antenna: Twin terminated folded dipole antenna for HF systems. 7th International conference on broadband Communications and biomedical applications. Davies, K. (1965). Ionospheric radio propagation. United States Department of Commerce, National Bureau of Standards.
- Edwards, D., & Cervera, M. (2022). Seasonal variation in land and sea surface backscatter coefficients at high frequencies. *Remote Sensing*, 14(21), 5514. https://doi.org/10.3390/rs14215514
- Edwards, D., Cervera, M., & MacKinnon, A. (2022). A comparison of the Barrick and backscatter ionogram methods of calculating sea surface backscatter coefficients. *Remote Sensing*, 14(9), 2139. https://doi.org/10.3390/rs14092139
- Ester, M., Kriegel, H.-P., Sander, J., & Xu, X. (1996). A density-based algorithm for discovering clusters in large spatial databases with noise Proceedings of the second International Conference on knowledge discovery and data mining, Portland, Oregon.
- Fabrizio, G. A. (2013). High frequency over-the-horizon radar: Fundamental principles, signal processing, and practical applications. MCGRAW-HILL Professional.
- Forsythe, V. V., Azeem, I., & Crowley, G. (2020). Ionospheric horizontal correlation distances: Estimation, analysis, and implications for ionospheric data assimilation. *Radio Science*, 55(12), e2020RS007159, https://doi.org/10.1029/2020RS007159
- Fridman, S. V., Nickisch, L. J., Aiello, M., & Hausman, M. (2006). Real-time reconstruction of the three-dimensional ionosphere using data from a network of GPS receivers. *Radio Science*, 41(5). https://doi.org/10.1029/2005RS003341
- Fridman, S. V., Nickisch, L. J., & Hausman, M. (2009). Personal-computer-based system for real-time reconstruction of the three-dimensional ionosphere using data from diverse sources. *Radio Science*, 44(3). https://doi.org/10.1029/2008RS004040
- Fridman, S. V., Nickisch, L. J., & Hausman, M. (2012). Inversion of backscatter ionograms and TEC data for over-the-horizon radar. *Radio Science*, 47(4). https://doi.org/10.1029/2011RS004932
- Friedrich, M., Pock, C., & Torkar, K. (2018). FIRI-2018, an updated empirical model of the lower ionosphere. *Journal of Geophysical Research:* Space Physics, 123(8), 6737–6751. https://doi.org/10.1029/2018JA025437
- Frissell, N. A., Baker, J. B. H., Ruohoniemi, J. M., Gerrard, A. J., Miller, E. S., Marini, J. P., et al. (2014). Climatology of medium-scale traveling ionospheric disturbances observed by the midlatitude Blackstone SuperDARN radar. *Journal of Geophysical Research: Space Physics*, 119(9), 7679–7697. https://doi.org/10.1002/2014JA019870
- Gillies, R. G., Hussey, G. C., Sofko, G. J., McWilliams, K. A., Fiori, R. A. D., Ponomarenko, P., & St.-Maurice, J. P. (2009). Improvement of SuperDARN velocity measurements by estimating the index of refraction in the scattering region using interferometry. *Journal of Geophysical Research*, 114(A7). https://doi.org/10.1029/2008JA013967
- Greenwald, R. A., Baker, K. B., Dudeney, J. R., Pinnock, M., Jones, T. B., Thomas, E. C., et al. (1995). DARN/SUPERDARN. Space Science Reviews, 71(1–4), 761–796. https://doi.org/10.1007/BF00751350
- Greenwald, R. A., Baker, K. B., Hutchins, R. A., & Hanuise, C. (1985). An HF phased-array radar for studying small-scale structure in the high-latitude ionosphere. *Radio Science*, 20(1), 63–79. https://doi.org/10.1029/RS020i001p00063
- Haldoupis, C. (2012). Midlatitude sporadic E. A typical paradigm of atmosphere-ionosphere coupling. Space Science Reviews, 168(1–4), 441–461. https://doi.org/10.1007/s11214-011-9786-8
- Haselgrove, J. (1955). Ray theory and a new method for ray tracing. In Physics of the ionosphere (pp. 355-5364). Physical Society.
- Hayashi, H., Nishitani, N., Ogawa, T., Otsuka, Y., Tsugawa, T., Hosokawa, K., & Saito, A. (2010). Large-scale traveling ionospheric disturbance observed by superDARN Hokkaido HF radar and GPS networks on 15 December 2006. *Journal of Geophysical Research*, 115(A6), A06309. https://doi.org/10.1029/2009JA014297

RUCK ET AL. 23 of 25

.wiley.com/doi/10.1029/2024SW003916, Wiley Online Library on [02/05/2025]. See the Terms

are governed by the applicable Creative Comm

- Hodos, T. J., Nava, O. A., Dao, E. V., & Emmons, D. J. (2022). Global sporadic-E occurrence rate climatology using GPS radio occultation and ionosonde data. *Journal of Geophysical Research: Space Physics*, 127(12), e2022JA030795. https://doi.org/10.1029/2022JA030795
- Hughes, J. M., Bristow, W. A., Greenwald, R. A., & Barnes, R. J. (2002). Determining characteristics of HF communications links using SuperDARN. Annales Geophysicae, 20(7), 1023–1030. https://doi.org/10.5194/angeo-20-1023-2002
- Jiang, W., Liu, E., Kong, X., Shi, S., & Liu, J. (2022). Zhongshan HF radar elevation calibration based on ground backscatter echoes. *Electronics Now*, 11(24), 4236. https://doi.org/10.3390/electronics11244236
- Karhunen, T. J. T., Robinson, T. R., Arnold, N. F., & Lester, M. (2006). Determination of the parameters of travelling ionospheric disturbances in the high-latitude ionosphere using CUTLASS coherent scatter radars. *Journal of Atmospheric and Solar-Terrestrial Physics*, 68(3–5), 558– 567. https://doi.org/10.1016/j.jastp.2005.03.021
- Koustov, A. V., Ullrich, S., Ponomarenko, P. V., Ghalamkarian Nejad, M., Themens, D. R., & Gillies, R. G. (2022). Occurrence rates of SuperDARN ground scatter echoes and electron density in the ionosphere. *Radio Science*, 57(11), e2022RS007520. https://doi.org/10.1029/ 2022RS007520
- Kunduri, B. S. R., Baker, J. B. H., Ruohoniemi, J. M., Thomas, E. G., & Shepherd, S. G. (2022). An examination of SuperDARN backscatter modes using machine learning guided by ray-tracing. Space Weather, 20(9), e2022SW003130. https://doi.org/10.1029/2022SW003130
- Kunduri, B. S. R., Erickson, P. J., Baker, J. B. H., Ruohoniemi, J. M., Galkin, I. A., & Sterne, K. T. (2023). Dynamics of mid-latitude sporadic-E and its impact on HF propagation in the North American sector. *Journal of Geophysical Research: Space Physics*, 128(9), e2023JA031455. https://doi.org/10.1029/2023JA031455
- Martyn, D. F. (1935). The propagation of medium radio waves in the ionosphere. Proceedings of the Physical Society, 47(2), 323–339. https://doi.org/10.1088/0959-5309/47/2/311
- Milan, S. E., Jones, T. B., Robinson, T. R., Thomas, E. C., & Yeoman, T. K. (1997). Interferometric evidence for the observation of ground backscatter originating behind the CUTLASS coherent HF radars. *Annales Geophysicae*, 15(1), 29–39. https://doi.org/10.1007/s00585-997-0029-y
- Munk, W. H., & Nierenberg, W. A. (1969). High frequency radar sea Return and the Phillips saturation constant. *Nature*, 224(5226), 1285. https://doi.org/10.1038/2241285a0
- Nishitani, N., Ogawa, T., Otsuka, Y., Hosokawa, K., & Hori, T. (2011). Propagation of large amplitude ionospheric disturbances with velocity dispersion observed by the SuperDARN Hokkaido radar after the 2011 off the Pacific coast of Tohoku Earthquake. *Earth Planets and Space*, 63(7), 891–896. https://doi.org/10.5047/eps.2011.07.003
- Nishitani, N., Ruohoniemi, J. M., Lester, M., Baker, J. B. H., Koustov, A. V., Shepherd, S. G., et al. (2019). Review of the accomplishments of mid-latitude super dual auroral radar network (SuperDARN) HF radars. Progress in Earth and Planetary Science, 6(1), 27. https://doi.org/10.1186/s40645-019-0270-5
- Oinats, A. V., Kurkin, V. I., & Nishitani, N. (2015). Statistical study of medium-scale traveling ionospheric disturbances using SuperDARN Hokkaido ground backscatter data for 2011. Earth Planets and Space, 67(1), 22. https://doi.org/10.1186/s40623-015-0192-4
- Oinats, A. V., Nishitani, N., Ponomarenko, P., & Ratovsky, K. G. (2016). Diurnal and seasonal behavior of the Hokkaido East SuperDARN ground backscatter: Simulation and observation. Earth Planets and Space, 68(1), 18. https://doi.org/10.1186/s40623-015-0378-9
- Perry, G. W., Ruzic, K. D., Sterne, K., Howarth, A. D., & Yau, A. W. (2022). Modeling and validating a SuperDARN radar's Poynting flux profile. Radio Science, 57(3), e2021RS007323. https://doi.org/10.1029/2021RS007323
- Ponomarenko, P., & McWilliams, K. A. (2023). Climatology of HF propagation characteristics at very high latitudes from SuperDARN observations. *Radio Science*, 58(5), e2023RS007657. https://doi.org/10.1029/2023RS007657
- Ponomarenko, P., Nishitani, N., Oinats, A. V., Tsuya, T., & St.-Maurice, J.-P. (2015). Application of ground scatter returns for calibration of HF interferometry data. Earth Planets and Space, 67(1), 138. https://doi.org/10.1186/s40623-015-0310-3
- Ponomarenko, P., St.-Maurice, J.-P., & McWilliams, K. A. (2018). Calibrating HF radar elevation angle measurements using E layer backscatter echoes. *Radio Science*, 53(11), 1438–1449. https://doi.org/10.1029/2018RS006638
- Ponomarenko, P. V., St. Maurice, J. P., Hussey, G. C., & Koustov, A. V. (2010). HF ground scatter from the polar cap: Ionospheric propagation and ground surface effects. *Journal of Geophysical Research*, 115(A10). https://doi.org/10.1029/2010JA015828
- Ponomarenko, P. V., Waters, C. L., & Menk, F. W. (2007). Factors determining spectral width of HF echoes from high latitudes. *Annales Geophysicae*, 25(3), 675–687. https://doi.org/10.5194/angeo-25-675-2007
- Ribeiro, A. J., Sterne, K., de Larquier, S., Reimer, A., Wessel, M., Rafiq, M., et al. (2020). vtsuperdarn/davitpy: Final release of davitpy (v0.9). Zenodo. https://doi.org/10.5281/zenodo.3824466
- Ruck, J. (2024a). SuperDARN Blackstone antenna gain patterns (version 1). [Dataset]. Zenodo. https://doi.org/10.5281/zenodo.10797004
- Ruck, J. (2024b). Validation of the IRI2016 ionospheric model using SuperDARN ground backscatter measurments. Companion data set for paper (version 1). [Dataset]. Zenodo. https://doi.org/10.5281/zenodo.10797245
- Ruck, J. J., & Themens, D. R. (2021). Impacts of auroral precipitation on HF propagation: A hypothetical over-the-horizon radar case study. Space Weather, 19(12), e2021SW002901. https://doi.org/10.1029/2021SW002901
- Samson, J. C., Greenwald, R. A., Ruohoniemi, J. M., Frey, A., & Baker, K. B. (1990). Goose Bay radar observations of Earth-reflected, atmospheric gravity waves in the high-latitude ionosphere. *Journal of Geophysical Research*, 95(A6), 7693–7709. https://doi.org/10.1029/JA095iA06p07693
- Shepherd, S. G. (2017). Elevation angle determination for SuperDARN HF radar layouts. Radio Science, 52(8), 938–950. https://doi.org/10.1002/2017RS006348
- Shim, J. S., Kuznetsova, M., Rastätter, L., Bilitza, D., Butala, M., Codrescu, M., et al. (2012). CEDAR Electrodynamics Thermosphere Ionosphere (ETI) Challenge for systematic assessment of ionosphere/thermosphere models: Electron density, neutral density, NmF2, and hmF2 using space based observations. Space Weather, 10(10). https://doi.org/10.1029/2012SW000851
- Shim, J. S., Kuznetsova, M., Rastätter, L., Hesse, M., Bilitza, D., Butala, M., et al. (2011). CEDAR electrodynamics thermosphere ionosphere (ETI) challenge for systematic assessment of ionosphere/thermosphere models: NmF2, hmF2, and vertical drift using ground-based observations. Space Weather, 9(12). https://doi.org/10.1029/2011SW000727
- Slimming, B., & Cervera, M. A. (2019). Calculation of high frequency land backscatter coefficients. Retrieved from https://www.dst.defence.gov.au/publication/calculation-high-frequency-land-backscatter-coefficients
- Sterne, K. T., Greenwald, R. A., Baker, J., & Ruohoniemi, J. M. (2011). Modeling of a twin terminated folded dipole antenna for the super dual auroral radar network (SuperDARN). 2011 IEEE RadarCon (RADAR), 934–938.
- SuperDARN Data Analysis Working Group. (2022). SuperDARN radar software toolkit (version 5.0). (Participating members: Thomas, E. G., Reimer, A. S., Bland, E. C., Burrell, A. G., Grocott, A., Ponomarenko, P. V., Schmidt, M. T., Shepherd, S. G., Sterne, K.T., Walach, M.-T.). [Software]. Zenodo. https://doi.org/10.5281/zenodo.801458

RUCK ET AL. 24 of 25



Space Weather

- 10.1029/2024SW003916
- Super Dual Auroral Radar Network. (2021a). SuperDARN 2014 RAWACF. [Dataset]. Federated Research Data Repository. https://doi.org/10. 20383/102.0452
- Super Dual Auroral Radar Network. (2021b). SuperDARN 2018 RAWACF. [Dataset]. Federated Research Data Repository. https://doi.org/10. 20383/101.0290
- Thayaparan, T., Marchioni, J., Kelsall, A., & Riddolls, R. (2020). Improved frequency monitoring system for sky-wave over-the-horizon radar in Canada. *IEEE Geoscience and Remote Sensing Letters*, 17(4), 606–610. https://doi.org/10.1109/LGRS.2019.2928172
- Themens, D. R., & Jayachandran, P. T. (2016). Solar activity variability in the IRI at high latitudes: Comparisons with GPS total electron content. Journal of Geophysical Research: Space Physics, 121(4), 3793–3807. https://doi.org/10.1002/2016JA022664
- Themens, D. R., Jayachandran, P. T., Bilitza, D., Erickson, P. J., Häggström, I., Lyashenko, M. V., et al. (2018). Topside electron density representations for middle and high latitudes: A topside parameterization for E-CHAIM based on the NeQuick. *Journal of Geophysical Research: Space Physics*, 123(2), 1603–1617. https://doi.org/10.1002/2017ja024817
- Themens, D. R., Jayachandran, P. T., Galkin, I., & Hall, C. (2017). The empirical Canadian high Arctic ionospheric model (E-CHAIM): NmF2 and hmF2. *Journal of Geophysical Research: Space Physics*, 122(8), 9015–9031. https://doi.org/10.1002/2017JA024398
- Themens, D. R., Jayachandran, P. T., & McCaffrey, A. M. (2019). Validating the performance of the empirical Canadian high Arctic ionospheric model (E-CHAIM) with in situ observations from DMSP and CHAMP. J. Space Weather Space Clim., 9, A21. https://doi.org/10.1051/swsc/2019021
- Themens, D. R., Jayachandran, P. T., McCaffrey, A. M., Reid, B., & Varney, R. H. (2019). A bottomside parameterization for the empirical Canadian high Arctic ionospheric model. *Radio Science*, 54(5), 397–414. https://doi.org/10.1029/2018RS006748
- Theurer, T. E., & Bristow, W. A. (2017). High-frequency radar ground clutter spatial correlation analysis: Transverse ionospheric drift velocity. *Radio Science*, 52(4), 461–478. https://doi.org/10.1002/2016RS006162
- Thomas, E. G., & Shepherd, S. G. (2022). Virtual height characteristics of ionospheric and ground scatter observed by mid-latitude SuperDARN HF radars. *Radio Science*, 57(6), e2022RS007429. https://doi.org/10.1029/2022RS007429
- Watson, C., Themens, D. R., & Jayachandran, P. T. (2021). Development and validation of precipitation enhanced densities for the empirical Canadian high Arctic ionospheric model. *Space Weather*, 19(10), e2021SW002779. https://doi.org/10.1029/2021SW002779

RUCK ET AL. 25 of 25